6 Nuclear Cardiology

Arthur Iain McGhie, K. Lance Gould, and James T. Willerson

Myocardial Perfusion Imaging

Physiologic Principles

Briefly, the underlying physiological principles of stress-rest perfusion imaging are as follows: at rest, coronary flow is normal even in the presence of a narrowing of up to 85% diameter stenosis (Fig. 6.1).[1] Stress, usually in the form of dynamic exercise or vasodilatation, results in an increase in coronary flow. In a normal coronary artery, flow increases 2- to 2.5-fold with dynamic exercise or by three- to four-fold with maximal coronary vasodilation.[2–6] However, the increase in flow in a stenosed coronary is attenuated. Despite an increase in flow proximally, there is an increase in the pressure gradient across the stenosis, resulting in a drop in pressure and flow distal to the stenosis. This causes a heterogeneous distribution of blood flow during stress, with a greater increase in myocardial perfusion in the area subtended by the normal coronary artery relative to the myocardium supplied by the stenotic artery. In certain circumstances, coronary flow may actually decrease distal to the stenosis, resulting in subendocardial ischemia. This phenomenon of *myocardial steal* may occur in two circumstances. In the presence of a severe coronary stenosis, the coronary pressure distal to the stenosis may decrease enough during stress that it is insufficient to perfuse the endocardium, resulting in subendocardial ischemia despite an increase in total flow in the proximal epicardial artery. This is sometimes referred to as *vertical steal.* Alternatively, in the presence of one or more diseased vessels with collaterals between their distal beds, there may be an unequal fall in the pressure between the two distal perfusion beds. This can result in blood being shunted away from the distal bed with the higher perfusion pressure to the one with the lower perfusion pressure. This is referred to as *horizontal steal,* and also can result in the production of subendocardial ischemia in the affected area.

Therefore, resting coronary flow or myocardial perfusion imaging at rest does not sensitively reflect the presence or severity of coronary artery disease. However, the capacity to increase flow to high levels in response to exercise stress or pharmacologic coronary arteriolar vasodilators, that is, *coronary flow reserve,* becomes impaired in the presence of coronary artery stenosis of moderate severity. Coronary flow reserve, illustrated in Figure 6.2, is defined as the ratio of maximum flow or perfusion during stress or pharmacologic vasodilation to resting flow or perfusion. Figure 6.3 relates stenosis severity (horizontal axis) to coronary flow reserve expressed as the relative increase of flow in multiples times the initial baseline resting flow (vertical axis). The dashed line indicates resting flow and the solid line is flow reserve. The gray zone indicates the range for multiple observations. With progressive narrowing, baseline flow remains normal until the coronary artery is narrowed by 80% to 85% diameter stenosis. However, coronary flow reserve begins to decrease at 40% to 50% diameter stenosis for a vasodilatory stimulus increasing flow normally to four times baseline. For a stimulus increasing flow to five or six times baseline levels, coronary flow reserve would be reduced by an even milder 30% diameter stenosis. For the experimental stenoses upon which Figure 6.3 was based, normal arterial diameter and stenosis length were constant and relatively uniform for each stenosis in a progressive series of experimental coronary artery constrictions. Consequently, percent narrowing related well to flow reserve with some data scatter (gray area of Fig. 6.3) due to variable physiologic conditions of heart rate and aortic pressure, which may alter flow reserve somewhat.[7] In humans, absolute dimensions and length stenoses are highly variable, with the consequence that percent diameter stenosis is poorly related to coronary flow reserve.[7–13] However, both experimentally and in humans, it has been shown that directly measured coronary flow reserve is equivalent to, interchangeable with, and predicted by the arteriographic geometry of coronary artery stenoses if all stenosis dimensions are accounted for including percent stenosis, absolute cross-sectional lumen area, length, and shape.[7,14–16]

Mechanisms Underlying Coronary Flow Reserve

To explain maintenance of normal resting coronary flow but reduced coronary flow reserve during progressive coronary

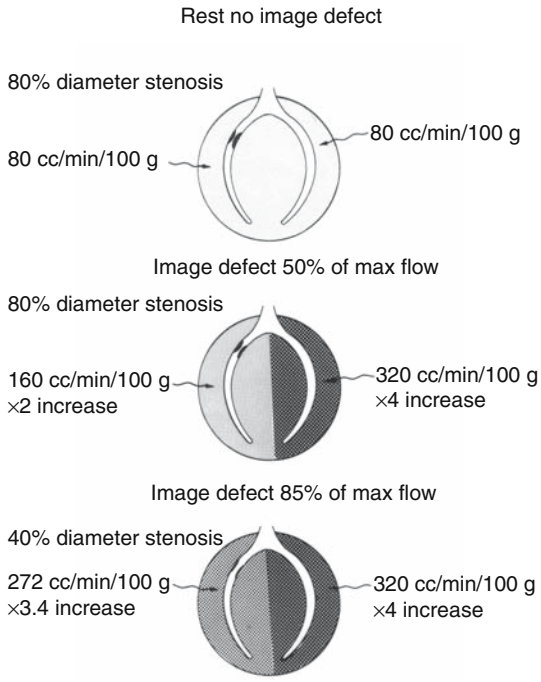

FIGURE 6.1. Principles for the detection of coronary artery disease with perfusion imaging under conditions of maximal coronary vasodilation. With an 80% diameter narrowing, coronary flow reserve is limited to an approximately twofold increase over resting levels compared with a fourfold increase in nonstenotic arteries. The abnormal area therefore has 50% less activity, reflecting 50% decrease in regional maximal flow compared with the normal maximum. A milder stenosis of approximately 40% diameter narrowing will produce a mild relative defect of approximately 15% below maximal flow, indicating a mild lesion.

constriction, consider the stenotic coronary artery as two resistances in series, that is, a narrowed tube and a distal coronary vascular bed, represented schematically in Figure 6.4. Normally, the distal coronary bed resistance at rest is high. In this schema, the driving pressure for flow is the total

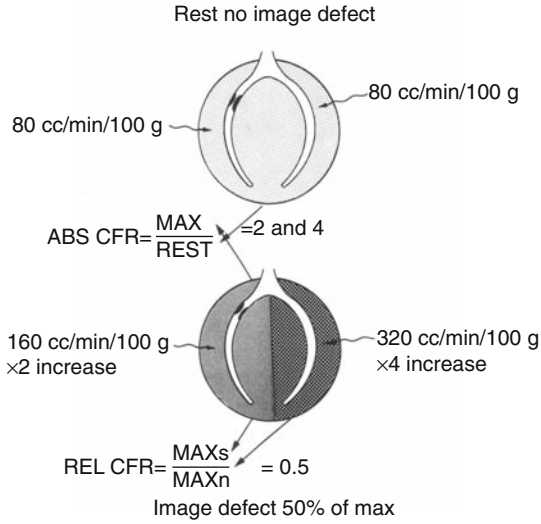

FIGURE 6.2. Concept of absolute coronary flow reserve (ABS CFR) and (REL CFR) relative coronary flow reserve.

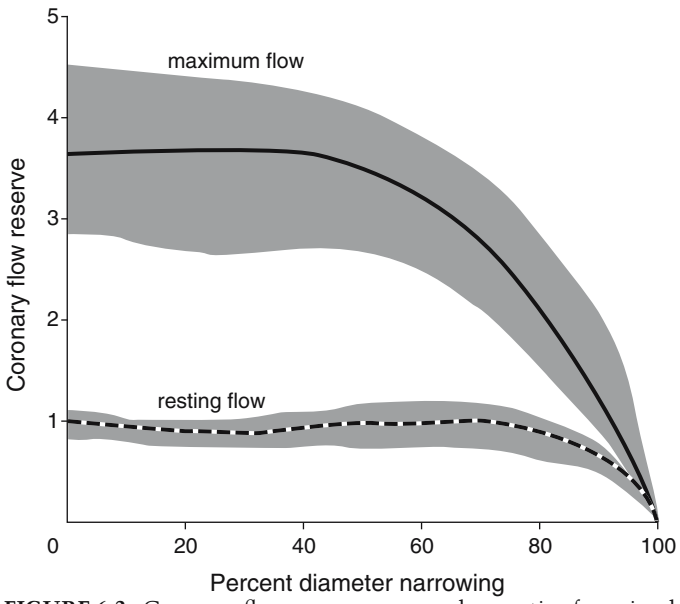

FIGURE 6.3. Coronary flow reserve expressed as a ratio of maximal flow to resting flow is given on the vertical axis, with percent diameter narrowing given on the horizontal axis. With progressive narrowing, resting flow does not change (dashed lines), whereas the maximal potential increase in flow or coronary flow reserve begins to fall at approximately 50% diameter narrowing. Shaded areas represent the limits of variability of data about the mean plotted by the solid and dashed lines.

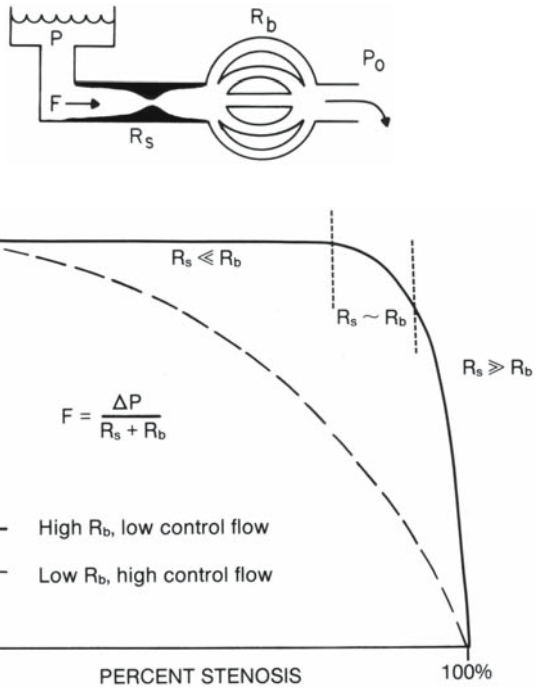

FIGURE 6.4. Diseased coronary circulation as two resistances in series. R_s indicates the resistance of the stenotic artery, and R_b indicates the resistance of the distal vascular bed. The effects of reducing R_b with the use of vasodilators are shown by the dashed line. The equation shows the relation between resistance and flow *(F)* for various segments of the curves. For a given total pressure gradient across the narrowed tube and distal vascular bed, flow is determined primarily by R_b if R_b is large. Changes in the stenotic resistance R_s have little effect until the value of R_s approaches that of R_b.

pressure gradient across the stenosis and distal vascular bed, which is approximately central aortic pressure since venous pressure is relatively small. Therefore, flow is determined approximately by aortic pressure divided by the sum of the resistances of the stenosis (R_s) and of the distal vascular bed (R_b) in series. If the distal bed resistance is large compared with the stenosis resistance, as normally found at rest, large changes in the stenosis resistance will have little effect on flow, which is determined primarily by distal vascular bed resistance. Therefore, a progressive stenosis up to a point will have no hemodynamic effect on resting coronary blood flow. However, as the stenosis becomes sufficiently severe to create a resistance comparable to that of the distal vascular bed, the distal bed vasodilates, loses its ability to autoregulate, and further narrowing causes a fall in resting coronary blood flow. When the stenosis becomes sufficiently severe that its resistance is much greater than that of the distal vascular bed, autoregulation will be lost and flow will be determined predominantly by the stenosis resistance alone. Further arterial narrowing then causes resting flow to fall as shown in Figure 6.4. Thus, the coronary vascular system is normally a low-flow, high-resistance circulation at rest. Coronary vasodilators or stress convert this normally low-flow, high-resistance system into a high-flow, low-resistance system in which coronary stenoses, even mild ones, limit maximum flow. Such logic explains why imaging regional myocardial perfusion at maximum coronary vasodilation can be used to detect coronary narrowing.

Absolute and Relative Coronary Flow Reserve

The concept of coronary flow reserve, defined as maximum flow divided (normalized) by resting control flow, has evolved into an accepted functional measure of stenosis severity since first proposed (Fig. 6.2).[7–13,17,18] Its validity has been confirmed and applied clinically by noninvasive imaging and by invasive methods. These clinical methods measure pharmacologically induced increases in coronary blood flow, most commonly with intravenous dipyridamole for noninvasive studies and intracoronary papaverine for invasive studies. More recently intravenous adenosine has been used.

However, changes in aortic pressure and heart rate are known to alter cardiac workload and therefore baseline coronary blood flow as well as altering maximum coronary flow under conditions of maximal vasodilation.[18] Consequently, absolute coronary flow reserve, as measured by flow meter, also varies with aortic pressure and heart rate independent of stenosis geometry due to differential effects of these variables on resting and maximal coronary flow. Under markedly varying physiologic conditions, or from patient to patient, absolute coronary flow reserve may not reliably or specifically reflect severity of coronary artery narrowing since it may be altered by physiologic factors unrelated to stenosis geometry.

In contrast, relative maximum coronary flow or relative flow reserve is defined as maximum flow in a stenotic artery divided (normalized) by the normal maximum flow in the absence of stenosis. During maximal coronary vasodilation physiologic variables, such as aortic pressure, heart rate, metabolic demand, and vasomotor tone alter distal coronary bed resistance equally for both normal and stenotic arteries. When the maximum flow in the stenotic artery is normalized by normal maximum flow, the effects of pressure, heart rate, or vasomotor tone on flow in the numerator and denominator of this ratio cancel out. Therefore, relative differences in regional maximum flow, or relative flow reserve, are determined primarily by geometric stenosis severity. Relative flow reserve, therefore, is a measure of stenosis severity relatively independent of physiologic variables.

Rather than considering absolute coronary flow reserve to be competitive or antithetical to relative flow reserve, these measurements are independent variables providing complementary information. Absolute flow reserve is the flow capacity of the stenotic coronary artery and vascular bed under whatever conditions of pressure, workload, hypertrophy, vasomotor tone, or stenoses are present. It reflects the cumulative summed effects of these various factors without being specific for the mechanism or cause of altered flow reserve. Relative coronary flow reserve reflects more specifically the effects of the stenosis independent of and not affected by the other physiologic variables if normal maximum flow is high enough. Thus, absolute and relative coronary flow reserve are complementary.

Single Photon Emission Tomography

Physics and Instrumentation

Use of radionuclides to image the heart depends on the ability to detect emitted electromagnetic radiation from injected radionuclides. The radionuclide is usually either taken up by the myocardium or remains in the intravascular compartment. The emitted gamma rays are detected by a scintillation counter where the emitted electromagnetic radiation is converted into electrical energy and transformed into a digital format to produce images either of myocardial activity or the cardiac blood pool.

Scintillation Counter

These counters are usually made of sodium iodide thallium [NaI(Tl)] activated crystal. The purpose of the scintillation crystal is to convert the energy of γ-radiation into visible light. When a γ-ray interacts with the atom in the crystal, a high-speed electron is produced. This electron in turn disturbs other atoms in its path, creating more high-speed electrons. The number of high-speed electrons generated is in proportion to the γ-ray's total kinetic energy. These electrons move through the crystal until trapped by an atom of thallium, when their kinetic energy is converted into a photon of light, that is, a scintillation. This whole process occurs within a microsecond of the initial interaction between the high-energy photon and the crystal. Every γ-ray absorbed by the crystal results in the production of a large number of photons, which is in direct proportion to the energy of the γ-rays.

Subsequently, a *photomultiplier* converts these photons of light into an electrical signal, which then amplifies the electrical signal. Photons of light are detected by the photo-

multiplier using a thin plate, called a *photocathode*, which releases electrons in proportion to the photons striking it. The electrons are then accelerated through a series of usually 10 plates, known as *dynodes*, which multiply the electrons striking them in proportion to voltage difference between the plates. This results in an amplification factor of approximately 1 million. Following this, the electrons are collected by an anode, and an electrical impulse is generated by a preamplifier. The energy of the γ-ray absorbed by the crystal and the subsequent light released by the crystal are directly proportional to the height of this electrical pulse, that is, voltage.

A device called a *pulse height analyzer* is used to preselect the range of energies to be counted (energy window) from the distribution of available energies (energy spectrum). Any energies corresponding to γ-rays with this predetermined energy window are rejected. Discriminating the energy of the γ-ray is important as it facilitates (1) selection of different radionuclides with different energies and (2) the elimination of less energetic γ-rays scattered by the patient's tissue prior to detection by the scintillation device. However, pulses generated by the unscattered γ-rays are not all of exactly the same amplitude, and they are distributed around the exact characteristic energy of the radionuclide (photopeak). The less spread of the radionuclide around the photopeak, the better the energy resolution of the system, and therefore the better the inherent counting and imaging characteristics of the device.

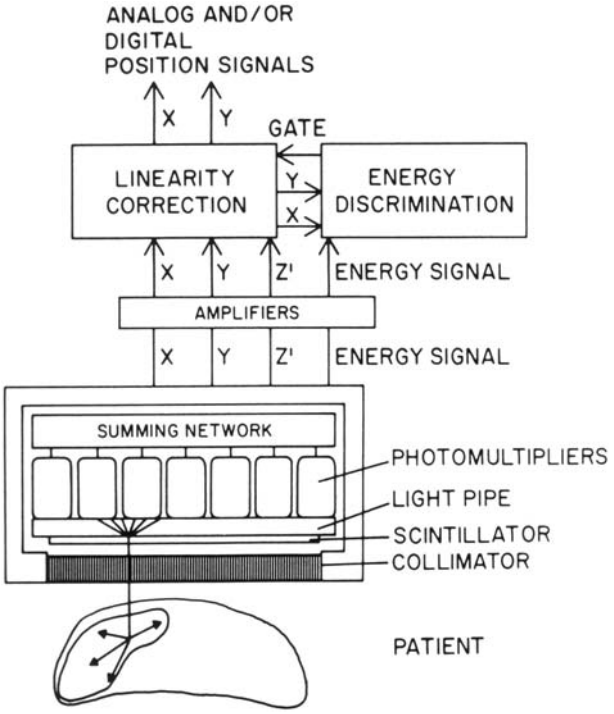

FIGURE 6.5. Schematic diagram of a gamma camera.

Single-Crystal Gamma Camera

This camera uses a large (300–500 mm), thin (75–125 mm) NaI(Tl) crystal with an array of photomultiplier tubes covering one side of the crystal. On the other side of the crystal is a lead plate with multiple holes in it called a *collimator* (Fig. 6.5). This causes selective interference by blocking those rays not traveling in the selected direction. In some ways, the collimator is analogous to the lens of a photographic camera resulting in a preselection of γ-rays before they strike the crystal. The most commonly used collimator in nuclear cardiology is a parallel-hole collimator. The lead septa between the holes absorb most of the γ-rays not traveling parallel to the holes. The larger the diameter or shorter the length of the holes, the higher is the sensitivity of the collimator, and the smaller the diameter or longer the length of the holes, the higher the spatial resolution of the collimator.

The γ-rays passing through the holes of the collimator strike the crystal and produce a scintillation. Photons produced by the scintillation are detected by all the photomultiplier tubes; photomultiplier tubes closer to the event gather more light than those farther away. All output from the photomultipliers is relayed into electronic computer circuitry where it is processed. A *positional analyzer* determines and assigns x and y Cartesian coordinates to the point in the crystal where the scintillation occurs. In addition, output of all the photomultipliers is summed, representing the total energy of the γ-ray that interacted with the crystal, to form an energy or z pulse. The z pulse is sent to the pulse height analyzer, and it is set to accept a preselected range of energies (see above). If the z pulse is within the predetermined range, it is referred to as either a trigger impulse or a signal (s) pulse. This signals that the scintillation event should be counted. Each time a trigger impulse is received by the cathode ray tube, it allows the emission of electrons from the electron gun. The x and y positional impulses are transmitted to the horizontal and vertical plates, creating a deflection in the path of the electrons corresponding to the scintillation coordinates. Electrons hit the phosphor screen of the cathode ray tube, creating a small scintillation that can be recorded on photographic film. However, today computers are used for image display, processing, analysis, and archiving purposes. Therefore, the x, y, and z pulses are also relayed to the computer interface unit. These impulses first must be converted from analog to digital format using an *analog-to-digital converter* (ADC). The ADC converts the pulse height into discrete numbers. The x and y impulses both have an ADC, whereas the z impulse signals the ADCs to convert the analog pulses to digital numbers.

The current generation of gamma cameras performs real-time corrections for (1) tube drift, (2) energy variations, and (3) spatial nonlinearity. *Tube drift correction* automatically adjusts the photomultipliers so that each one generates the same pulse voltage when it gathers photons from the same light source. This correction is required because the earth's magnetic field affects the photomultiplier's output as a function of its angle and is particularly important in rotational tomography. The *energy correction factor* compensates for differences in response of individual photomultiplier tubes, differences in the crystal, or differences in regional light-

gathering properties. Energy-specific field floods need to be acquired periodically to generate the time-dependent energy maps. This predetermined map is then applied by a correction circuit in real time. This normalizes the relationship of the energy window to the shape of the spectrum, practically abolishing the variations in energy response. *Linearity correction* is required because the gamma camera positioning scheme does not perfectly image straight radioactive line sources. A phantom of straight lines in horizontal and vertical positions is imaged. The displacement is measured and stored, allowing the linearity circuit to correct lines so that they appear perfectly straight in the image.

Acquisition Modes

Planar acquisition is the simplest means of acquisition, where the γ-camera acquires data in one dimension in multiple projections, usually in three, that is, anterior, left anterior oblique, and left lateral projection. Right anterior and left posterior oblique projections may be obtained depending on the circumstances. Despite obtaining multiple projections, the spatial resolution is limited. This occurs because of overlapping activity from either noncardiac structures or overlap between normal and abnormal segments within the heart. For example, the presence of adjacent pulmonary activity may overlap the posterolateral wall in the left anterior oblique, making the anteroseptum appear hypoperfused; alternatively, a small perfusion defect may not be detected because of activity in normal myocardium in an adjacent but different plane.

Tomographic acquisition, also known as single photon emission computed tomography (SPECT), is now the most common acquisition mode for myocardial perfusion imaging. A series of planar images are obtained usually in a 180-degree rotation from 45 degrees right anterior oblique (RAO) to 45 degrees right posterior oblique (RPO). Using a technique called *filtered backprojection*, a computer creates a set of transaxial images from these planar images, allowing the radioisotope distribution to be displayed in three dimensions. From these transaxial images horizontal and vertical long axis sections and short axis sections are constructed. This results in improved contrast and enhanced spatial resolution, when compared to planar imaging. However, this technique is more exacting, in terms both of equipment and acquisition technique, and of requiring more rigorous quality control.

Filtered backprojection uses an algorithm that is dependent on the fact that each photon that interacts with the crystal must pass through the collimator, which defines the path of the photon because the holes in the collimator are parallel. The reconstruction algorithm back-projects or sends back the counts from their recorded position on the crystal, along a line perpendicular to the face of the crystal (Fig. 6.6). The back-projected lines cross at the origin of the radiation, and these points are recorded in computer memory from which tomograms are generated. However, the reconstruction algorithm deposits counts in each pixel along the back-projected line, producing a star-shaped artifact and in-plane blurring of the image. To reduce these artifacts, the images are modified by a filter that eliminates unwanted low- and high-frequency statistical noise, hence the term *filtered backprojection*.

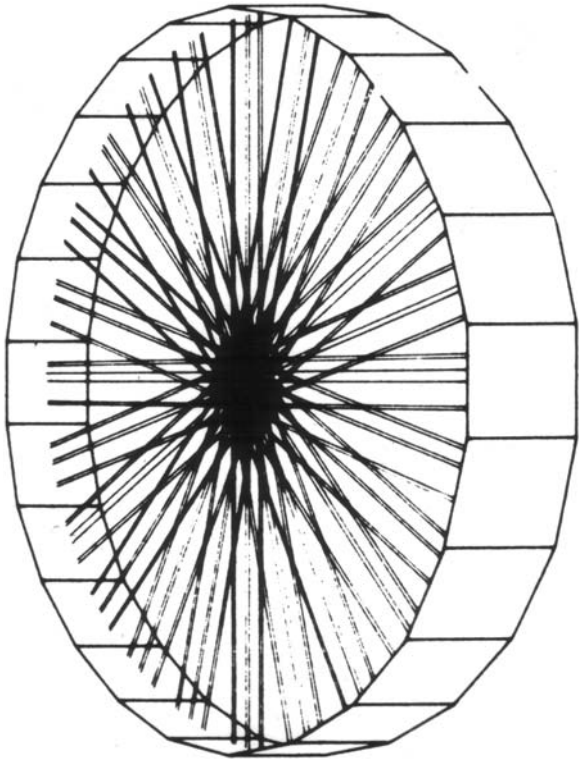

FIGURE 6.6. Schematic representation of the process of backprojection. Multiple planar views are taken around 360 degrees or 180 degrees, with data being back-projected in space to define the origin of the data in space (see text for further details).

Radiopharmaceuticals

^{201}Thallium

This cation is a potassium analog and was the first widely used radioisotope in the assessment of myocardial perfusion. Myocardium uptake occurs by both active and passive mechanisms involving Na,K–adenosine triphosphatase (ATPase).[19,20] Uptake of ^{201}thallium (^{201}Tl) by the myocyte is not affected by either ischemia or hypoxia unless these processes result in cell death.[21–24] There is a linear relationship between ^{201}Tl uptake and coronary blood flow, with a tendency to underestimate and to overestimate at the upper and lower limits of the physiologic range, respectively.[25–28] Thallium washes out of the myocardium by diffusion with a half-life in the myocardium of 4 to 8 hours. The rate is primarily dependent on the ^{201}Tl concentration gradient between the myocardium and blood.[29,30]

In comparison to a normal coronary artery, lower coronary flow rates are achieved in a stenosed artery during stress. As a consequence, there is less ^{201}Tl uptake by the myocardium in this artery's distribution. Following stress, coronary flow returns to baseline levels and is the same in *both* the normal and stenosed artery. However, because of

the unequal distribution of ^{201}Tl in the myocardium during stress, clearance of ^{201}Tl is heterogeneous. The greater concentration gradient between the normal myocardium and blood results in a higher washout rate of ^{201}Tl than in the hypoperfused myocardium where the ^{201}Tl concentration gradient is less. As a consequence, there is a trend for the myocardial concentration of ^{201}Tl to equalize with time in the normal and abnormally perfused myocardium. Therefore, there is apparent "redistribution" of ^{201}Tl, with the stress-induced perfusion defect apparently reversing during rest imaging 3 to 4 hours later. A perfusion defect following stress that has resolved by time of distribution imaging is considered to represent ischemic and viable myocardium.

Conversely, a defect still present at the time of redistribution imaging was classically interpreted as representing nonviable scar tissue. However, several studies, using either improvement in regional ventricular function following revascularization or myocardial uptake of ^{18}fluorine-fluorodeoxyglucose (FDG), have identified viable myocardium in 40% to 60% of fixed ^{201}Tl perfusion defects.[31–33] Several studies from Bonow and associates[34–36] have shown that either performing late–24-hour redistribution imaging or reinjecting an additional dose of ^{201}Tl after 4-hour redistribution in the presence of an apparent "fixed" perfusion defect results in reversibility of a significant proportion of these defects, and that this correlates with myocardial uptake of FDG. The same workers were able to show that areas of hypoperfused myocardium, where the reduction in ^{201}Tl uptake is only mild or moderate, that did not redistribute are still viable.[37] However, Kitsiou and associates[38] have shown that although mild-to-moderate perfusion fixed defects contain viable myocardium, these areas are less likely to show functional improvement after revascularization than mild-to-moderate defects that are reversible.

^{99m}Technetium-Labeled Perfusion Agents

^{99m}Technetium (^{99m}Tc)-labeled radiopharmaceuticals were developed in the early 1980s. Three agents, sestamibi, teboroxime, and tetrofosmin, are approved for clinical use by the United States Food and Drug Administration. In comparison to ^{201}Tl, ^{99m}Tc-labeled radiopharmaceuticals offer significant advantages, including (1) a shorter 6-hour half-life, which allows a larger patient dose to be administered, typically 25 to 35 mCi compared to 3 to 4 mCi of ^{201}Tl; and (2) higher energy, 140 for ^{99m}Tc photons versus 74 keV for ^{201}Tl, reducing the scatter fraction and resulting in superior energy discrimination. These advantages typically translate into higher quality images.[39,40]

Teboroxime has kinetic properties that are different from the other currently available ^{99m}Tc-labeled radiopharmaceuticals. It is extremely lipophilic, and myocardial uptake correlates closely with coronary blood flow over a wide range of flow rates and has very rapid myocardial washout.[41] Unlike ^{201}Tl, teboroxime washout is largely flow dependent, and it appears that the rate of washout from the myocardium may allow differentiation between viable and nonviable tissue.[42–44] Theoretically, it may be possible to evaluate stress and resting myocardial perfusion with one injection at maximal stress. However, the short residence time in the myocardium mandates rapid data acquisition, and failure to do so may potentially lead to image artifacts because of the changing myocardial distribution of ^{99m}Tc-teboroxime during acquisition. Despite the initially encouraging clinical results of ^{99m}Tc-teboroxime,[45] its rapid clearance made it very difficult to use in the clinical arena, resulting in preference for the other ^{99m}Tc-labeled radiopharmaceuticals and the subsequent withdrawal of the product from the marketplace by the manufacturer.

In contrast, the kinetics of sestamibi are in many ways at the opposite end of the spectrum to teboroxime. It is a lipophilic cation that accumulates in the myocardium in proportion to blood flow, although at higher coronary flow rates the relationship becomes nonlinear, resulting in an underestimation of coronary flow. It has a first-pass extraction fraction of 65%, which is lower than either ^{201}Tl or teboroxime. However, its net extraction is higher because it is avidly retained by myocytes with little bidirectional exchange of sestamibi with minimal redistribution and slow clearance.[46] The volume of distribution for sestamibi is so large that saturation of myocardial uptake does not occur. Uptake occurs primarily by diffusion, resulting primarily from negative electrical gradients across sarcolemmal and inner mitochondrial membranes, and to a lesser extent concentration gradients.[47] Carvalho and associates[48] demonstrated that 90% of ^{99m}Tc-sestamibi in vivo activity is associated with mitochondria as the original free cationic complex.

Clinical studies to date indicate that imaging with ^{99m}Tc-sestamibi has demonstrated a similar degree of accuracy for the overall detection of coronary artery disease, but usually results in higher quality images and is more accurate for the detection of individual coronary artery stenoses.[34,49] Use can be made of ^{99m}Tc-sestamibi's long myocardial retention time, which allows for a patient to be imaged up to 4 to 6 hours after administration of ^{99m}Tc-sestamibi. This has been useful in triaging patients presenting to the emergency room with chest pain and also in evaluating therapeutic interventions in the setting of acute myocardial infarction where ^{99m}Tc-labeled radiopharmaceutical can be given acutely, with imaging to be performed later when the patient is in a more stable condition and environment.[50–55] The higher count rates and the lack of redistribution also allow gated tomographic acquisitions to be performed. This increases the accuracy of the technique and allows the evaluation of endocardial wall motion and myocardial thickening, providing important information on regional and global ventricular function.[56–58]

Tetrofosmin is the most recent ^{99m}Tc-labeled radiopharmaceutical approved for clinical use. Like its predecessor, ^{99m}Tc-sestamibi, tetrofosmin is a lipophilic cation, which diffuses across the sarcolemmal and mitochondrial membranes.[59–61] Similar to sestamibi, tetrofosmin tends to underestimate flows greater than 2 mL/min/g and to overestimate flows less than 0.2 mL/min/g.[62] Munch and colleagues[63] reported that ^{99m}Tc-tetrofosmin had a shorter myocardial half-life and higher heart-liver ratios than ^{99m}Tc-sestamibi. In a canine model using adenosine, Glover and associates[64] observed that ^{99m}Tc-tetrofosmin uptake underestimated the flow heterogeneity more than ^{201}Tl. A clinical study[65] com-

paring ^{99m}Tc-tetrofosmin with ^{201}Tl SPECT imaging using dipyridamole stress had findings that tended to support those reported by Glover and associates. In this clinical study, ^{201}Tl imaging identified more reversible defects than ^{99m}Tc-tetrofosmin SPECT imaging, and in addition, the authors noted that the magnitude of reversible perfusion defects also was more severe in the ^{201}Tl images. Similar findings have also been reported by others.[66,67] However, in general terms, clinical experience has shown that tetrofosmin is comparable to the other currently available myocardial perfusion agents.[68–70]

Choice of Stress

Exercise

The cardiovascular response to dynamic exercise results in an increase in cardiac output. The peripheral resistance decreases in active muscles and increases in resting tissues; overall there is a fall in systemic vascular resistance.[71] There is an increase in heart rate in response to exercise, mediated by alterations in the autonomic nervous system. The increase is linearly related to workload and oxygen uptake. The heart rate response to maximal dynamic exercise is dependent on many factors, especially the individual's age and health. The increases in cardiac output during dynamic exercise increases systolic arterial blood pressure, with little alteration in the diastolic pressure. Dynamic exercise is the most commonly used means of stress when using nuclear techniques. The procedure is carried out in a manner almost identical to conventional exercise electrocardiography. In addition, the patient should have an intravenous cannula placed in a large vein in the antecubital fossa prior to stress. At peak exercise, the patient is injected with the radiopharmaceutical and continues exercising for a further 60 to 90 seconds. The timing of imaging following exercise is dependent on the particular radiopharmaceutical being used.

Vasodilator Pharmacologic Stress

Pharmacologic stress is being increasingly used. The main indication for its use is when the patient is unable to exercise adequately. Reasons for this are varied and include concomitant medical conditions, such as peripheral vascular disease, morbid obesity, and neurologic disease; poor motivation; and antianginal medication (in particular β-adrenergic and calcium channel antagonists). It is also indicated for stressing patients with left bundle branch block (LBBB) or a paced rhythm because of the problem of artifactual reversible septal perfusion defects when exercise stress is used.

Dipyridamole is widely used in conjunction with myocardial perfusion imaging and has a similar diagnostic accuracy to exercise imaging.[72–74] Dipyridamole is a highly basic and hydrophobic pyrimidine derivative that induces an increase in endogenous adenosine levels by blocking uptake of adenosine by red cells and endothelium.[75–77] The increased concentrations of adenosine in the interstitial fluid results in relaxation of vascular smooth muscle. This may be mediated by a number of possible mechanisms, including (1) an inhibition of slow inward calcium current resulting in decreased calcium uptake, (2) activation of adenylate cyclase through A_2-receptors in smooth muscle cells, and (3) possible modulation of sympathetic neurotransmission.[78,79] Dipyridamole may alter systemic hemodynamics with a slight fall in blood pressure and slight increases in the heart rate and pressure-rate product. Once adenosine leaves the interstitium, it undergoes rapid intracellular metabolism via adenosine kinase by phosphorylation to adenosine monophosphate or deamination by adenosine deaminase.[80] Dipyridamole undergoes hepatic biotransformation to a monoglucuronide and is excreted in the bile.[81] Patients should be in a fasting state and should not have taken any xanthine medications (theophylline) in the previous 36 hours and caffeine beverages (including decaffeinated coffee or tea and cola) in the preceding 24 hours. It is contraindicated in patients with a history of significant reversible airways obstruction. An infusion of 0.142 mg/kg/min of dipyridamole is given over 4 minutes and with the radiopharmaceutical being administered 3 to 4 minutes later. Continuous clinical, electrocardiographic, and blood pressure monitoring is performed during the procedure, with imaging being performed in the usual manner. Serious adverse reactions have been reported following intravenous dipyridamole, including fatal and nonfatal myocardial infarction, ventricular fibrillation, symptomatic ventricular tachycardia, transient cerebral ischemia, and bronchospasm.[69] The effects of dipyridamole are usually rapidly reversed by the administration of aminophylline, which antagonizes the effects of adenosine at the A_2-receptor.[82] Side effects are reported in approximately 50% of patients following intravenous dipyridamole at the dose of 0.568 mg/kg. Chest pain occurs in approximately 15% to 40% and ST segment depression in 5% to 20% of patients. The presence of either or both does not reliably predict the presence of angiographically significant disease, although it is more common in their presence. Noncardiac symptoms are relatively common and include flushing, nausea, light-headedness, and mild headaches.

Adenosine, the mediator of dipyridamole's vasodilating action, is a powerful coronary arterial vasodilator.[83,84] Maximal coronary vasodilatation is obtained with an intravenous infusion rate of 100 to 140 μ/kg/min. This increases coronary blood flow velocity by 4.4-fold. The effects are maximal 2 minutes after the onset of the infusion and return to baseline within 2 to 3 minutes of its discontinuation. It is widely used as a pharmacologic stress and has a comparable diagnostic accuracy when compared with dipyridamole myocardial perfusion imaging.[85–87] The short half-life of adenosine results in it being better tolerated by patients. Verani's group[88] reported their experiences with this technique in 607 patients. Small but significant mean increases in heart rate and falls in the systolic and diastolic blood pressures were observed. First- and second-degree atrioventricular (AV) block occurred in 10% and 4% of patients, respectively; ischemic ST segment depression was identified in 13% of cases. Side effects were frequent but well tolerated; flushing occurred in 35%, chest pain in 34%, headache in 21%, and dyspnea in 19% of patients. In the majority of patients, the side effects ceased rapidly after terminating the adenosine infusion. The side effects were severe in only 2% of patients, and in only six of 607 patients was it necessary to discontinue the

infusion. No serious adverse reactions were reported. Recent studies of selective adenosine A_{2A}-receptor agonists have shown that the vasodilator effects of adenosine can be obtained without many of the side effects.[89–91]

Vasodilator stress imaging can be supplemented with exercise, using either isometric handgrip or low-level treadmill exercise.[92,93] The former has been used quite extensively following evidence of increased coronary flow when used in combination with dipyridamole.[94] But later data, using Doppler-derived indices of flow, have produced conflicting evidence.[6] Therefore, it probably confers benefit by different mechanisms, including an increase in afterload or vasoconstriction of small to moderate-sized arteries. Exercise also improves image quality by improving target-to-background ratios,[95,96] probably by causing splanchnic vasoconstriction.

Sympathomimetic Pharmacologic Stress

Dobutamine is a potent sympathomimetic agent with stimulatory effects on β_1-, β_2-, and α_1-adrenoreceptors with predominantly inotropic and a lesser chronotropic effects.[97,98] Therefore, dobutamine produces an increase in myocardial oxygen requirement by causing an increase in myocardial contractility and systolic blood pressure and at higher doses an increase in heart rate. The dose for dobutamine is usually 10 µg/kg/min increased by increments every 3 to 5 minutes to a maximal infusion rate of 30 to 40 µg/kg/min. Side effects that can occur with this agent include palpitation, headache, paresthesia, nausea, tremor, ventricular arrhythmia, and marked ST segment depression. Side effects usually resolve rapidly following discontinuation of the infusion. The effects of dobutamine are similar to those of dynamic exercise, and in the presence of coronary artery disease myocardial ischemia may be provoked.[99,100] It produces an increase in coronary flow of between two- and threefold, which is less than is typically seen with either dipyridamole or adenosine.[101] Studies indicate that dobutamine stress myocardial perfusion has clinical utility; however, it is usually reserved for patients with a contraindication to adenosine or dipyridamole.[102–105]

Imaging Protocols

Over the years different imaging protocols have been developed with the advent of new radiopharmaceuticals with different kinetics and the use of different pharmacologic stress agents. The American Society of Nuclear Cardiology (ASNC) has published guidelines in an effort to standardize imaging protocols.[106]

Choice of Stressor

If the patient can exercise adequately, exercise is preferred over pharmacologic stress in most circumstances. Adequate exercise is achieved when the patient achieves more than 85% of his maximum predicted heart rate for age and exercises of an adequate period of time, that is, longer than 6 minutes on a Bruce protocol. Circumstances where pharmacologic stress is preferred is when the patient will not exercise adequately to attain these goals for whatever reason, for example, arthritis, deconditioning, neurologic disease, or peripheral vascular disease. The presence of LBBB or a paced ventricular rhythm is an indication for vasodilator stress because of the reversible septal perfusion defects that can be produced by abnormal ventricular activation. In addition, pharmacologic stress is generally utilized when stress myocardial perfusion imaging is performed in the setting of a recent unstable angina or myocardial infarction, because of the relative lack of effect on hemodynamics. The main role of dobutamine in nuclear cardiology is when the use of dipyridamole or adenosine is contraindicated, usually in a patient with reversible obstructive airways disease.

^{201}Thallium

Typically 3 mCi of ^{201}Tl is injected at peak stress and imaging is commenced early, within 10 to 15 minutes, because of the kinetics of ^{201}Tl. A second set of images is acquired approximately 4 hours later after redistribution has occurred. If incomplete redistribution has occurred and myocardial viability is a clinical concern, then either a second injection of 1.5 mCi can be given and the patient reimaged 10 to 30 minutes later (reinjection imaging) or alternatively the patient can be reimaged 24 hours later. Thallium images are increasingly being acquired as electrocardiogram (ECG)-gated images to provide functional data in addition to perfusion. If ^{201}Tl imaging is being performed primarily to assess viability rather than stress-induced ischemia, then a rest-redistribution protocol is used. In this protocol, 3 mCi of ^{201}Tl is injected at rest with imaging being performed 15 to 30 minutes later and again at 4 hours, with the option of obtaining a 3rd set of images after 24 hours.

^{99m}Tc-Labeled Radiopharmaceuticals

The most widely used protocol for this group of pharmaceuticals is the same-day rest-stress protocol. Typically 8 to 9 mCi are injected at rest with imaging being performed approximately 1 hour later. The patient is stressed around 1 to 4 hours following the rest injection and receives around 25 to 30 mCi at peak stress. The stress images are acquired 15 to 60 minutes later; if the patient has been exercised, then imaging can be acquired 15 minutes after stress; however, if pharmacologic stress has been utilized, then imaging is delayed 45 to 60 minutes to allow for hepatic and visceral clearance of the radiopharmaceutical. The same-day stress-rest protocol involves performing stress imaging first using the smaller 8 to 9 mCi dose, with rest imaging being performed 1 to 4 hours later using the 25 to 30 mCi dose. This has the advantage that if the stress images are normal, then rest imaging does not need to be performed. However, it has the disadvantage that the stress images are acquired using the lower dose of the ^{99m}Tc labeled radiopharmaceutical and therefore may be of lower quality, which may adversely affect the diagnostic accuracy of the images. The third protocol that is used is a 2-day protocol with the rest and stress images being acquired on separate days. This protocol is particularly useful in two particular situations. The first is when imaging is being performed for diagnostic purposes, usually in patients with a low pretest likelihood, in which the stress portion is performed first

and if these images are normal, rest imaging is not required. The second application is in obese patients to maximize image quality by using the higher dose of the ^{99m}Tc radiopharmaceutical (0.31 mCi/kg) for both the rest and the stress images.

Hybrid Protocols

The other protocol that is widely used is the dual-isotope protocol. In this protocol, 2.5 mCi of ^{201}Tl is injected at rest with rest images being acquired 10 minutes later. Then the patient is stressed and 25 mCi of ^{99m}Tc-labeled radiopharmaceutical is injected at peak stress, with the stress images acquired 15 to 90 minutes later depending on the stressor used. If a fixed perfusion defect is seen, then 24-hour ^{201}Tl imaging can be performed. The main disadvantage of the technique is the greater interpretive skill required to read the images because of the differences between the rest and stress images resulting from differences in the physical properties of ^{201}Tl and ^{99m}Tc.

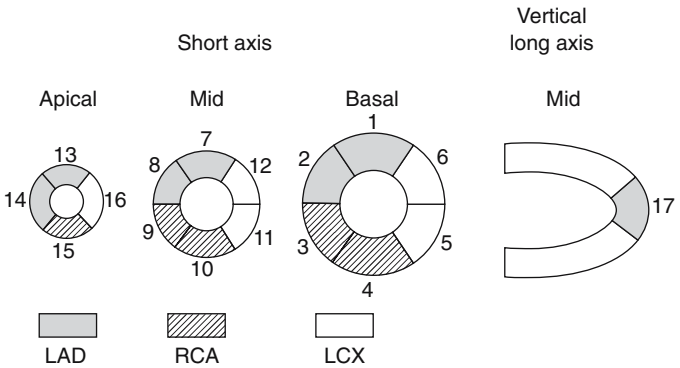

FIGURE 6.7. Schematic diagram showing the standardized segmentation and assignment of the coronary artery territories. LAD, left anterior descending; RCA, right coronary artery; LCX, left circumflex coronary arteries.

Analysis of Images

For the most part, tomographic imaging has replaced planar techniques because of enhanced contrast and spatial resolution and consequently improved sensitivity for the identification and localization of coronary artery disease.[107] The myocardial territories subtended by the left anterior descending coronary artery consist of the apical, anterolateral, anterior and anteroseptal portions of the left ventricle; the left circumflex coronary artery supplies the middle and posterior portions of the left ventricular wall, and the right coronary artery supplies the apical, inferior, and inferoseptal aspects of the left ventricle (Fig. 6.7). Figure 6.8 demonstrates ^{201}Tl tomograms following exercise and redistribution from a patient with disease of the left anterior descending and right coronary arteries. There are moderate-severe perfusion abnormalities involving both the anterior and septal as well as the inferior, inferoseptal, and inferolateral aspects of the left ventricle. In addition, there is evidence of left ventricular

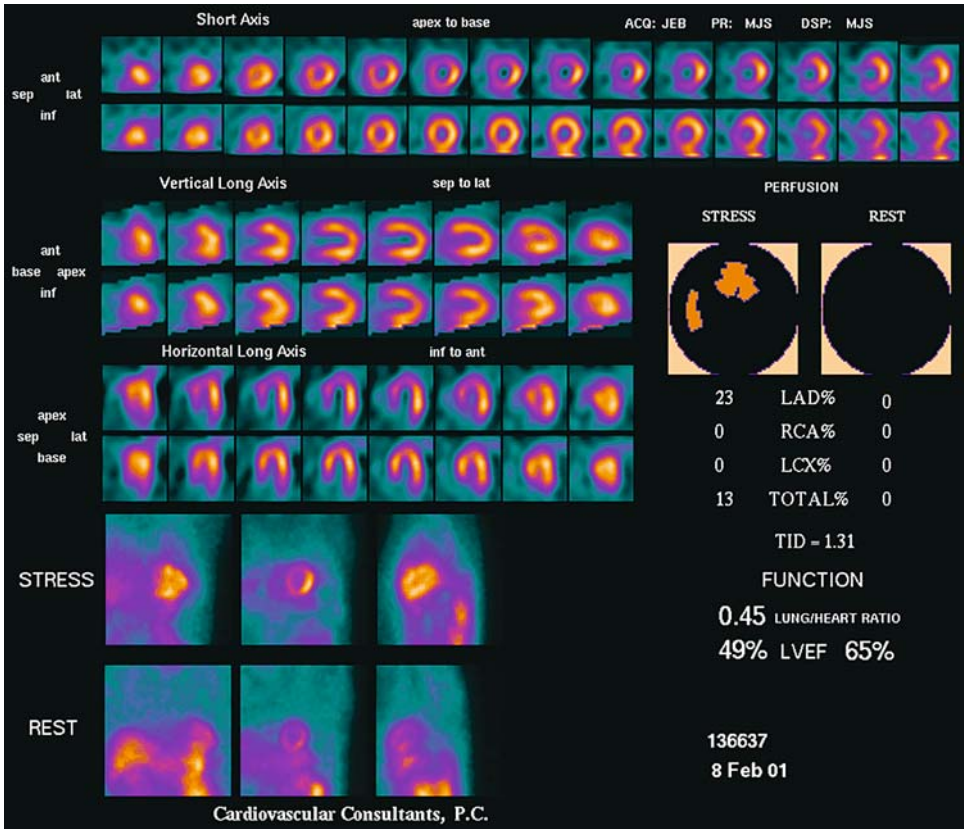

FIGURE 6.8. Exercise-redistribution of ^{201}Tl from a patient with disease of the left anterior and right coronary arteries. Representative short, vertical long, and horizontal tomograms are shown following exercise and redistribution. Perfusion defects are present in the anterior and septal walls indicative of left anterior descending coronary (LAD) ischemia as well as the inferior, inferoseptal, and inferolateral walls indicative of right coronary ischemia (RCA). In addition, there is transient dilatation of the left ventricle and a fall in the ejection fraction with exercise indicative of stress-induced left ventricular dysfunction.

decompensation with stress as manifested by transient dilatation of the left ventricle and a fall in the left ventricular ejection fraction with stress.

Interpretation of the images begins with analyzing the raw projection sets looking for potential factors that may result in image artifacts, for example, diaphragmatic or breast attenuation, and patient motion. Then, the reconstructed tomograms are evaluated for the presence of perfusion defects, including the severity (extent and intensity) of defects, and their location with respect to specific coronary distributions. The gated tomograms are also reviewed for global and regional function both at rest and following stress. Other markers of increased risk such as transient dilatation of the left ventricle poststress and, in the case of ^{201}Tl imaging, increased lung uptake are noted. Semiquantitative scoring is widely used in the analysis of images, where one representative apical, middle, and basal short axis section and one vertical short axis section at rest and following stress are scored according to the severity of the perfusion defect. From this analysis, a sum stress score, sum rest score, and a sum difference score are generated.[108] Semiquantitative analysis of images using this technique provides important prognostic information.[109] There are important gender-related differences in tissue attenuation that need to be taken into account when interpreting images. In males, the anterior and lateral segments normally demonstrate the highest relative activity, with the posterior and septal segments demonstrating lower activity. In contrast, females normally demonstrate somewhat higher activity in the inferoposterior segments as compared to the anterior and lateral segments.[110] Subjective analysis of images is usually also supplemented with computer analysis. Quantitative computer techniques for the analysis of tomograms evaluate the extent and severity of the defects and the amount of reversibility present. Improvement sensitivity with only marginal effects on specificity are found when computer-generated analysis is combined with the qualitative visual evaluation of the images.[111–113] The results of these computer-generated analyses are usually displayed as polar maps or "bull's eye" displays (Fig. 6.9). The center of the polar map is obtained from an apical short axis section, with subsequent short axis sections being obtained from progressively more basal portions of the left ventricle, with the most basal short axis section forming the outer border of the polar map. Polar maps are divided into approximately 100 segments. The profiles from the patient's segments are compared to a data bank of gender-matched normal profiles previously acquired from a group of normal individuals (usually patients with <5% probability of coronary disease). Any of the patient's segments falling 2.5 standard deviations below the normal mean value are plotted (Fig. 6.10).

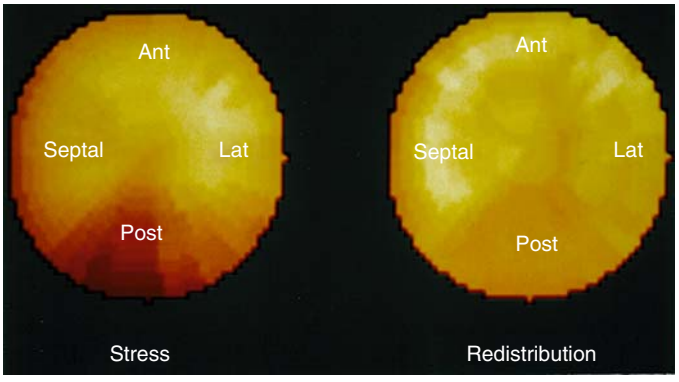

FIGURE 6.9. Polar maps from a patient with right coronary artery disease (see Color Plates 5 to 6). There is hypoperfused area involving the inferior and posterolateral aspects of the left ventricle in the stress map. The redistribution map shows that this is almost completely reversible. Ant, anterior; Lat, lateral; Post, posterior.

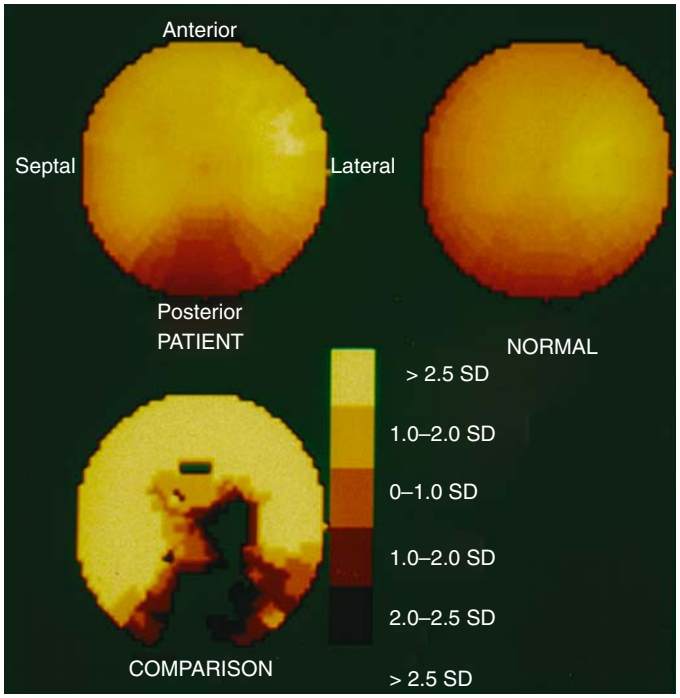

FIGURE 6.10. The patient's polar map (top left) is compared with normal polar map (top right) obtained from patients with less than a 5% likelihood of coronary artery disease. Areas that are outside of 2.5 standard deviations (SDs) of normal are blacked out (bottom left).

Recognition of image artifacts is very important when interpreting SPECT myocardial perfusion images. Many factors have been identified as potentially causing artifacts, including patient motion, soft tissue attenuation (breast tissue, lateral chest wall fat, diaphragm), overlying visceral activity, LBBB, left ventricular hypertrophy, reconstruction artifacts, flood field nonuniformity, and center of rotation errors.[114] Breast tissue attenuation is a common occurrence, and results in a lower count density in the anterior wall of the left ventricle of women (anterior/inferior count density ratio = 1.0 in women and 1.2 in men). Diaphragmatic attenuation results in perfusion abnormalities involving the inferior wall of the left ventricle and can be minimized by imaging the patient in the prone position.[115] Motion during acquisition is a common cause of image artifacts. This can occur following exercise resulting from the phenomenon sometimes referred to as "upward-creep." This results from changes in depth of respiration from deep to shallower

breathing resulting in the heart "creeping" up in the thorax during the acquisition. Delaying the start of imaging for 10 minutes after cessation of exercise usually eliminates this phenomenon. Patient motion during acquisition may result in the production of factious perfusion abnormalities, and can usually be easily identified by examining a cine display of the planar projection images.[116] One of the advantages of using Tc-labeled radiopharmaceuticals is that it allows for repeat imaging, as there is no change in the myocardial distribution with time, unlike ^{201}Tl. Therefore, if a patient moves, then the acquisition can be repeated, or if diaphragmatic attenuation is identified, the imaging can be repeated using the prone position. Most gamma-camera manufacturers provide software packages that will help correct for patient motion. The presence of LBBB can result in septal perfusion abnormalities, which may be reversible when exercise is used for stress and can usually be avoided by using vasodilator pharmacologic stress.[117]

The use of ECG-gated acquisitions (see Radionuclide Ventriculography, below, for details on electrocardiographically gated acquisitions) during myocardial perfusion imaging provides important incremental data over static imaging. There has been an exponential increase in its use over the last 10 years, with currently approximately 80% of studies being performed using ECG-gated acquisition compared to only 3% in 1993.[118] Initially, it was thought that this type of acquisition could only be performed using ^{99m}Tc-labeled radiopharmaceuticals because of the higher count rates. However, it has been shown that it is also possible to acquire ECG-gated SPECT images using ^{201}Tl.[119] The additional ECG-gated data provide important information regarding regional and global ventricular function, including wall thickening, ventricular volumes, and ejection fraction both at rest and following stress. In addition, the use of gated images appears to improve the specificity of the technique by better differentiating between attenuation and scar in "fixed" perfusion defects.

Another important development in SPECT imaging that is under continuing evaluation and refinement is the use of attenuation correction techniques to minimize the effects of breast and diaphragmatic attenuation artifacts. Several studies have evaluated the effect of attenuation correction on the accuracy of stress myocardial perfusion imaging.[120–126] The findings from these studies are summarized in Table 6.1.[127] These studies have shown that attenuation correction does result in an improvement in diagnostic accuracy, mainly from improvement in specificity, and also an increase in interpretative confidence. The combination of attenuation corrected and ECG-gated images does appear to result in an increase in diagnostic accuracy, with improvements in both sensitivity and specificity. Most gamma-camera manufacturers now offer attenuation correction options on their imaging equipment and both the ASNC and the Society of Nuclear Medicine have concluded that attenuation correction is a useful adjunct to myocardial perfusion imaging.[128] Despite this, the technology to date has not been widely applied in clinical practice. The reasons for this are likely multifactorial, but include the added cost of the equipment, increased technical knowledge and quality assurance required to successfully implement the technology, and lack of reimbursement for attenuation correction.

TABLE 6.1. Comparative diagnostic accuracy of attenuation-corrected and nonattenuation-corrected single-photon emission computed tomography

	Sensitivity		*Specificity*		*Normalcy*	
First author	***NC***	***AC***	***NC***	***AC***	***NC***	***AC***
Ficaro[121]	78%	84%	46%	82%	88%	98%
Hendel[125]	76%	78%	44%	50%	86%	96%
Links*[126]	84%	88%	69%	92%	69%	92%
Gallowitsch[124]	89%	94%	69%	84%	NA	NA
Ficaro†[122]	93%	93%	84%	88%	78%	85%

*Includes motion correction and depth dependent blur correction.

†Includes scatter correction.

AC, attenuation-corrected single photon emission computed tomography (SPECT); NA, not available; NC non–attenuation-corrected SPECT.

Positron Emission Tomography: Assessment of Myocardial Perfusion

Basic Principles

A positron is a positively charged particle with the same mass as an electron but with a positive charge. They are emitted along with a neutrino by certain unstable atoms, usually elements with a low atomic number, in the process of radioactive decay. The positron travels 1 to 3 mm in tissue before colliding with an electron. When this occurs both the positron and the electron are *annihilated*, with conversion of their combined mass into electromagnetic γ-radiation. Two photons are given off, each with an energy of 511 keV, that travel in opposite directions at approximately 180 degrees to each other. When a photon pair is detected by a pair of radiation detectors, connected through an electrical coincidence counting circuit, an annihilation event is recorded. This circuit is set so that one decay is recorded only if both detectors are activated simultaneously (within 4 to 10 nanoseconds) by the photon pair. All other events are rejected. Therefore, radioactive decays occurring outside the sample volume between the detectors are excluded from the count data since an unpaired photon striking only one of the detectors is not counted. Therefore, collimation is accomplished electronically with coincidence counting, rather than with lead collimators, as in single-photon imaging. The electronic collimation of coincidence counting provides higher efficiency and better count statistics resulting in positron emission tomography's (PET) superior spatial and contrast resolution to that of SPECT systems.

Generically, PET cameras contain 1000 to 1500 detectors in three to eight banks of rings, attached to photomultiplier tubes (PMTs) in ratios ranging from one to eight detectors for each PMT. Scintillations from the coincidence detectors are converted to electronic signals from the PMTs that are subsequently converted to digital information; then the data are stored and processed on a computer to reconstruct a tomographic image using filtered backprojection. A transmission image for attenuation correction is obtained by placing a ring of activity around the patient for imaging the target organ

before injection of radiotracer. The positron radiotracer is then injected intravenously and an emission image obtained by backprojection techniques. The emission image is corrected for attenuation loss, random coincidences, scattered radiation, dead-time losses, and variation in detector sensitivity. The burgeoning role of PET imaging in oncology has resulted in increased availability of PET/computed tomography (CT) scanners, which have presented interesting options for their use in the field of cardiovascular medicine.[129] These scanners have the potential to facilitate evaluation of both the coronary anatomy from CT coronary angiography and myocardial perfusion, with PET providing both anatomic and physiologic data.

Positron-Emitting Radiopharmaceuticals

Several positron-emitting radioisotopes are used in cardiac PET imaging. Typically, these have a short physical half-life (rubidium-82, $t_{1/2}$ = 76 seconds; oxygen-15, $t_{1/2}$ = 2.1 minutes; carbon-11, $t_{1/2}$ = 20.4 minutes; nitrogen-13, $t_{1/2}$ = 10 minutes; fluorine-18, $t_{1/2}$ = 110 minutes) when compared to conventional single-photon–emitting isotopes (Fig. 6.11). The short half-life minimizes radiation to the patient and enables sequential studies to be performed over a short period of time. In addition, O-15, C-11, F-18, and N-13 can be incorporated into metabolic substrates used by the heart, facilitating evaluation of the metabolic processes of the myocardium in vivo. However, synthesis of these radiolabeled substrates is technically complex and demands both a radiochemist and an on-site cyclotron. Rubidium-82 is an exception; it is generator produced from the parent compound strontium-82, which has a half-life of 25 days and is available commercially.

Evaluation of Myocardial Perfusion

Myocardial perfusion can be evaluated using either a diffusible tracer, such as O-15–labeled water, or by using an extractable tracer, such as Rb-82– or N-13–labeled ammonia. Experimentally it has been shown that there is a very close correlation between the myocardial distribution of microspheres and O-15–labeled water over a wide range of coronary flows.[130,131] As O-15–labeled water labels both the cardiac pool and the myocardium, the blood pool activity is subtracted using O-15–labeled carbon monoxide which labels the red blood cells. Although this technique has been used successfully in clinical studies, it is technically demanding and is not used in routine clinical practice.

The extractable tracers, Rb-82– and N-13–labeled ammonia, have been widely used in clinical practice.[7,14,16,17,132–134] For imaging purposes, it is assumed that these tracers are distributed to and retained by the myocardium in relation to coronary blood flow; however, this is not the case. Myocardial uptake of N-13–labeled ammonia is nonlinear, starting to plateau at coronary flow rates greater than 2.5 to 3.0 mL/g/min.[135] However, the relative high first-pass extraction (60–70%), rapid blood clearance, and comparatively long myocardial retention time results in very good quality images. Typically, 10 to 5 mCi of N-13 ammonia is injected at rest; after a 4-minute delay to allow for blood pool clearance, rest images are acquired with stress images being acquired 40 minutes after the first injection of N-13–labeled ammonia. The myocardial uptake of Rb-82 is also nonlinear with coronary blood flow, with an underestimation of flows greater than 2.5 to 3.0 mL/g/min, and it has a first-pass extraction of 50% to 60%. However, it does have the advantage of being generator produced and readily available commercially, and

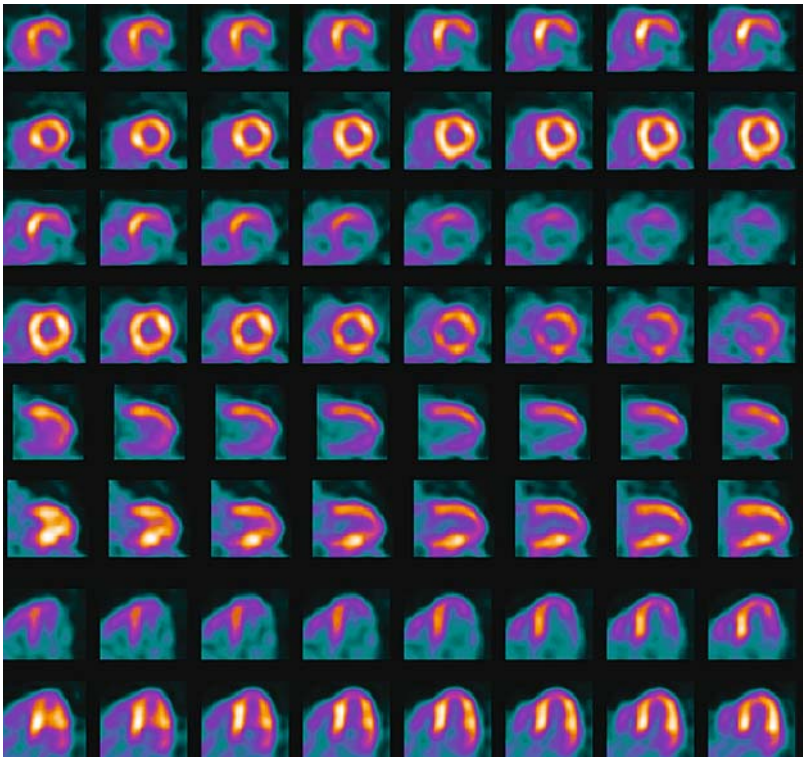

FIGURE 6.11. Rubidium-82 images from a patient showing multivessel ischemia. A severe reversible perfusion defect involving the inferior, inferolateral, and inferoseptal walls of the left ventricle consistent with ischemia in the left circumflex and right coronary arteries. In addition, there is a reversible defect involving the anterior and anterolateral walls indicative of ischemia in the left anterior descending coronary distribution.

its short high-life means that rest and stress imaging can be performed back to back in rapid succession resulting in a complete study being acquired in 30 to 60 minutes. However, the short half-life does mandate that pharmacologic stress be used. Generally, 30 to 50 mCi of Rb-82 are injected in a volume of 10 mL over 20 to 30 seconds with a fresh generator; later, toward the end of the generator life (4 weeks), 30 to 40 mL are required to deliver a similar dose of Rb-82. Emission data are acquired over 5 to 8 minutes with the second, stress dose being administered 10 minutes later during the dipyridamole or adenosine infusion (Fig. 6.11).

Evaluation of Myocardial Metabolism

The most widely evaluated and used labeled compounds are F-18–labeled fluorodeoxyglucose (FDG), carbon-11–labeled palmitate, and carbon-11–labeled acetate. F-18–labeled FDG is the most clinically utilized radiolabeled substrate and is used for assessment of myocardial viability. The relatively long half-life of F-18 means that although it is cyclotron-produced, it can be shipped to PET facilities without access to an on-site cyclotron. Under fasting conditions, fatty acids are the main energy source for normal myocardium; however, in the presence of ischemia, the myocardium increases its utilization of glucose as its source for high-energy phosphates. This enhanced utilization of glucose in ischemic myocardium can be detected by F-18 FDG-PET imaging. The radiolabeled intermediary undergoes phosphorylation by the hexokinase reaction, but cannot be metabolized any further in the glycolytic pathway. Hence, the phosphorylated FDG is trapped within the cytosol of the myocardium and accumulates in proportion to exogenous metabolism of glucose.[136,137] As discussed above, fatty acids are the preferred substrate under fasting conditions and account for 90% of oxygen consumed under aerobic conditions, and for this reason carbon-11–labeled palmitate has been used extensively to evaluate myocardial metabolism.[138–142] The uptake of the palmitate is primarily dependent on blood flow. Thereafter, clearance C-11 palmitate is biexponential, with an early fast component that reflects fatty acid β-oxidation and a second slower component that results from incorporation of the fatty acids into the endogenous lipid pool. In the presence of myocardial ischemia, β-oxidation is reduced and therefore clearance of C-11 palmitate is reduced, with a corresponding increase in the proportion of fatty acids being incorporated into the lipid pool.[143,144]

C-11–labeled acetate has been used to evaluate oxidative phosphorylation.[145–149] The myocardial avidly extracts acetate and is activated to acetyl–coenzyme A (CoA) in the cytosol and then is oxidized in the mitochondria via the tricarboxylic acid cycle, which is the final common pathway for oxidative metabolism. The clearance of this radiolabeled intermediary of myocardial metabolism is also biexponential. The rapid early phase reflects oxidative phosphorylation, while the slower, later phase reflects incorporation of the acetate into the amino acid and lipid pool. Rate constants calculated from the rapid, early clearance phase correlate closely with the rate of myocardial oxygen consumption over a wide range of physiologic values. In the presence of myocardial ischemia, uptake is reduced in proportion to blood flow and the clearance is reduced in proportion to the reduction in oxidative metabolism.[150,151]

Comparison of SPECT and PET Perfusion Imaging

There are several theoretical reasons to believe that PET is more accurate than its single photon counterpart. First, the intrinsic resolution of this technology affords higher resolution images. Second, the ability to correct for attenuation using a transmission scan should also improve the diagnostic accuracy of the technique. It should be remembered, however, that there is the potential for the production of image artifacts.[152] The main disadvantages of the PET technology are its limited availability and the significantly higher capital expenditure and running and maintenance costs.

Early studies from the 1980s evaluating PET in the diagnosis of coronary artery disease indicated that this technique was accurate for diagnosing coronary artery disease.[153–155] Three comparative trials in the 1990s suggested that PET had a superior diagnostic accuracy to SPECT imaging.[141,156,157] However, the evidence was not conclusive; one study did not demonstrate any statistically significant difference; another, which showed significantly higher sensitivity and specificity, has been criticized for its methodology and analysis.[158] The recent resurgence of interest in cardiac PET imaging, resulting from the increased availability of PET scanners from increased oncologic use, has brought the issue of the utility of cardiac PET imaging in clinical practice to the fore again. In a recent study, comparing contemporary PET and SPECT imaging techniques, PET was found to outperform SPECT imaging, with sensitivities of 81% and 75%, $p = .34$; specificities of 93% and 58%, $p = .0001$; and diagnostic accuracies of 86% and 68%, $p = .002$, for PET and SPECT, respectively.[159]

Radionuclide Ventriculography

Radionuclide ventriculography is one of the most widely used techniques for evaluating ventricular function. This essentially noninvasive method of assessing ventricular function can be easily performed and provides a reproducible, accurate evaluation of both right and left ventricular function. There are basically two methods of performing radionuclide ventriculography.

First-Pass Radionuclide Angiocardiography

This technique involves following the passage of a radioactive tracer through the central circulation. It requires the use of a gamma camera with a high count rate capability, usually 1×10^5 to 5×10^5 counts per second. This high count rate capability is optimally provided by a multicrystal gamma camera, for example the Baird-Atomic, which is both expensive and can be used solely for first-pass imaging studies. However, some of the current digital single crystal Anger gamma cameras have improved count rate capabilities and are reputed to provide satisfactory count statistics.

The radioisotope is administered as a *compact* bolus, 1 mL plus 20 mL saline flush, through a large vein, usually antecubital or jugular.[160] An anterior or 30-degree right

anterior oblique projection is used to optimize separation of the atria from the ventricles. The former is preferred because the position is more reproducible, it enhances resolution by minimizing the distance between the detector and the chest wall, and during exercise studies motion artifact is minimized by pressing the chest wall firmly against the detector. The right and left ventricles overlap in these projections; however, this does not pose a problem during the first pass of the radionuclide bolus. Data are usually acquired in a series of images with high temporal resolution. The optimal framing interval is determined by the sensitivity of the camera and the patient's heart rate. For example, when using a multicrystal gamma camera during an exercise study, the framing interval will be 25 msec. In a patient with normal hemodynamics, the whole first-pass transit is encompassed by 600 frames. The most commonly used radiopharmaceutical is ^{99m}Tc, complexed either to diethylenetriamine pentaacetic acid (DTPA) or sulfur colloid. This enables optimal excretion of the isotope via the kidneys to decrease background accumulation, which is an important consideration if more than one study is being performed.[161] Clinical studies using ^{195}gold (Au) have found it to be a suitable alternative to ^{99m}Tc.[162,163] The half-life of ^{195}Au is only 30.5 seconds, allowing multiple studies to be performed without imposing a prohibitive radiation burden on the patient or increasing background activity that occurs with ^{99m}Tc.

Following acquisition of the data, right and left ventriculograms are constructed from which ejection fractions and ventricular volumes can be calculated.[164] A number of time-activity curves are obtained; the number depends on the time taken for the bolus to traverse the chamber of interest, usually five to ten individual beats in a normal patient. The count rate reaches a maximum at end-diastole when ventricular volume is largest and falls in proportion to the ventricular volume to reach a minimum at end-systole. Data from individual beats are summed to provide a single curve, which is then corrected for background. The ejection fraction and ventricular volumes are then calculated from the normalized, background corrected time-activity curve (Fig. 6.12).

The first-pass technique has the advantage of excellent image contrast and chamber separation because of the absence of background activity from adjacent great vessels and organs, in particular the lung. In addition, acquisition time is short, usually between 20 and 30 seconds, which is an advantage for an exercise study's acquisition of data only during peak exercise. The first-pass technique also provides a means for the detection and quantitation of intracardiac shunts.[165–168] For both right-left and left-right shunts, the time-activity curves that are generated resemble dye-dilution curves and are analyzed using a similar methodology. Despite these advantages, it does have significant limitations. First, one is limited to two to three acquisitions per patient study because of the increasing radiation exposure to the patient and the increasing background activity. Second, the technique is more demanding both on personnel and equipment: (a) it requires a compact bolus injection; (b) any patient motion or ventricular arrhythmia, for example, coughing or one ventricular ectopic beat occurring during acquisition, can seriously degrade the radionuclide data; and (c) it requires the use of a multicrystal gamma camera or a digital Anger camera with high count rate capabilities. Additionally, evaluation of regional wall motion function is poorer in comparison to the gated equilibrium technique.

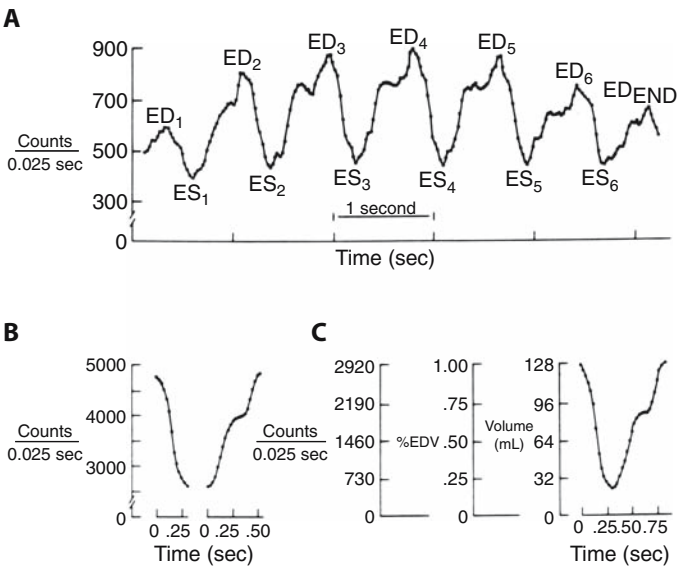

FIGURE 6.12. Calculation of left ventricular ejection fraction and volumes from first-pass radionuclide angiocardiography. (A) Uncorrected counts measured within the left ventricular region of interest during the levophase. (B) Summed systolic and diastolic segments. (C) Final volume curve after normalization and background correction. ED, end-diastole; ES, end-systole; EDV, end-diastolic volume.

Gated Equilibrium Radionuclide Ventriculography

In this technique, the patient's red blood cells are labeled with 25 to 35 mCi of ^{99m}Tc-pertechnetate, using either an in vivo or in vitro method. The in vitro or modified in vitro methods result in a consistently higher labeling efficiency. Scintigraphic data are acquired using a conventional single crystal Anger gamma camera in multiple planar projections. Usually an anterior, left anterior oblique and left lateral or posterior oblique are acquired (Fig. 6.13). The left anterior oblique (LAO) that best separates the right and left ventricles is chosen, that is, the best septal projection. The detector is also angled to separate the left atrium from the left ventricle. The anterior projection is usually at 45 degrees less than the best septal projection, and the left lateral projection is usually at 45 degrees more oblique than the best septal projection. In addition, the scintigraphic data are acquired gated to the electrocardiogram, with each R-R interval being divided equally into a predetermined number of time bins, usually 16 to 32 time bins (Fig. 6.14). During acquisition, scintigraphic data are stored in memory in one of these time bins, such that at the end of the acquisition each time bin will contain scintigraphic data from numerous, typically 300, R-R intervals (Fig. 6.15).

Gated equilibrium radionuclide ventriculography is one of the most accurate means of assessing ventricular function and can be easily performed using readily available

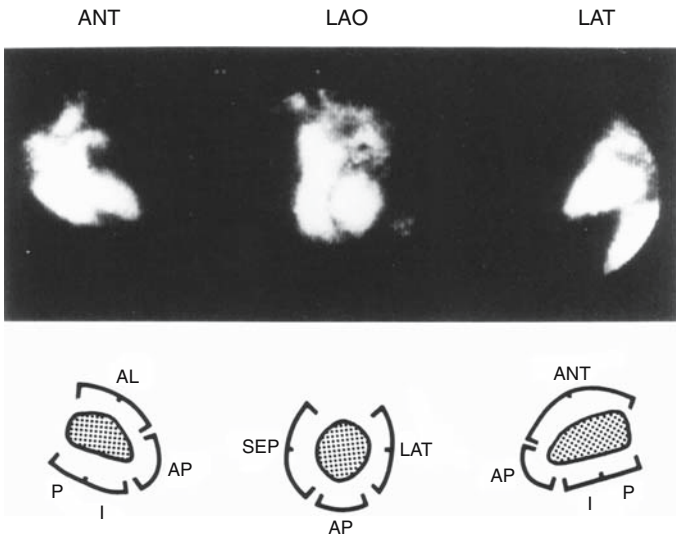

FIGURE 6.13. Assessment of regional left ventricular function from a gated radionuclide ventriculogram. Anterior (ANT), left anterior oblique (LAO), and left lateral (LAT) projections in end-diastole are shown. Corresponding segmentation is given below. AL, anterolateral: AP, apical; I, inferior; P, posterior; SEP, septal; LAT, lateral.

nuclear imaging systems. It facilitates acquisition of multiple projections or multiple studies up to 6 hours after administration of the isotope. The high count densities achieved, typically 300 counts/cm^2 in the left ventricle, enable an evaluation of region wall motion that is superior to the evaluation possible with the first-pass technique. The technique does have some limitations: (1) overlap between cardiac chambers, which can usually be resolved using multiple views; (2) limited spatial resolution, when compared to contrast ventriculography or echocardiography; and (3) longer acquisition times when compared to first-pass techniques, a minimum of 2 minutes, which can pose a problem during exercise studies in patients with limited or unpredictable exercise capabilities.

Many of these problems can be resolved by tomographic gated radionuclide ventriculography by providing an accurate three-dimensional representation of the entire cardiac blood pool.[169–171] Using this technique, all chambers are separated in space, which enables assessment of very limited ventricular segments without concern about adjacent and potentially superimposed segments. This technique provides an accurate means for assessing both global and regional ventricular function with a higher diagnostic accuracy than either contrast or planar radionuclide ventriculography.

Exercise Radionuclide Ventriculography

Exercise radionuclide ventriculography is performed using either the first-pass or gated equilibrium techniques. The commonly used gated-equilibrium technique is described here. A resting study is performed in the usual manner, but performing the left anterior oblique projection last, with the patient lying supine on a specially designed bicycle table-ergometer that has adjustable shoulder restraints and handle bars to minimize movement of the patient's torso during exercise. After obtaining the resting left anterior oblique projection, exercise is commenced. The exercise test is performed in exactly the same manner as with other exercise

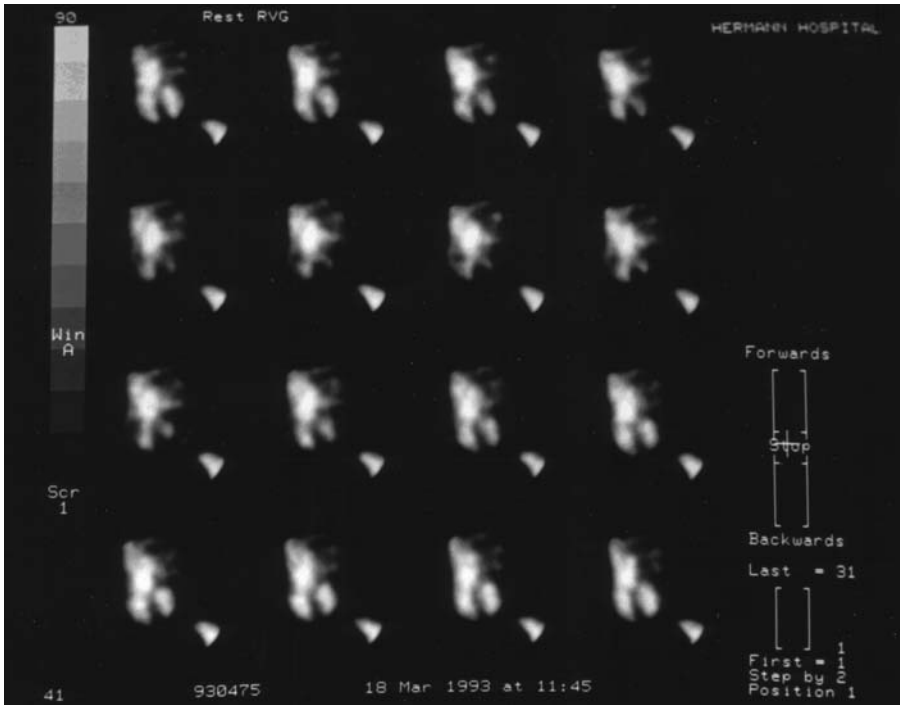

FIGURE 6.14. Sixteen frames from a gated radionuclide ventriculogram in the "best septal" left anterior oblique projection. The end-diastolic frame is the first image, located in the upper left of the figure; the end-systolic frame is the eighth image of the series.

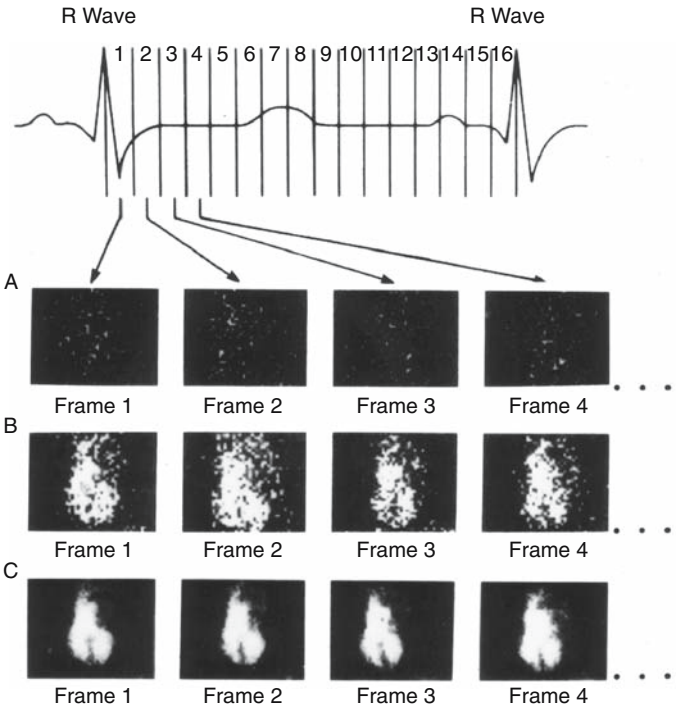

FIGURE 6.15. Schema explaining the principle of electrocardiographic-gated acquisition in radionuclide ventriculography. The cardiac cycle is divided into equal intervals (16 in this example). Counts recorded during each interval are stored in different computer frames. After a single cardiac cycle (row A), there are no recognizable images. After 20 cardiac cycles (row B), the images begin to be recognizable. After 400 cardiac cycles (300,000 counts per frame), image quality has improved considerably (row C).

tests, with continual monitoring of the electrocardiogram, heart rate, and blood pressure. Typically, the first stage of exercise is performed at 200 kilo/pound/meters (kpm) for 3 or 4 minutes and increased by 200-kpm increments (less if patient has a limited exercise capacity) to a symptom-limited maximum. Scintigraphic data are acquired during the last 2 minutes of each stage of exercise, when the hemodynamics have equilibrated. The hemodynamic response is different from that with erect exercise.[172,173] During supine exercise, there is less increase in end-diastolic volume and heart rate, but a greater increase in systolic blood pressure when compared to erect exercise. This does not appear to adversely affect the sensitivity of the technique.[174] There are significant gender-related differences in the left ventricular response to exercise. Women have a greater increase in end-diastolic volume and less increase in left ventricular ejection fraction in comparison to men.[175,176]

Analysis of Radionuclide Ventriculograms

Data from radionuclide ventriculograms can be used to provide many parameters of ventricular function. The method is relatively independent of geometric assumptions because there is complete mixing of the ^{99m}Tc-labeled red cells in the intravascular compartment, and the activity within the ventricle is proportional to ventricle volume.[177]

Left ventricular ejection fraction (LVEF) is calculated using the left anterior oblique projection by drawing a region of interest (ROI) around the left ventricle in end-diastole and end-systole. After correcting the counts in the ROIs for background activity, the ejection fraction is calculated from the formula

$$LVEF = EDc - ESc/EDc$$

where *EDc* and *ESc* are end-diastolic and end-systolic counts corrected for background, respectively.

Ventricular volumes can be calculated using a nongeometric count-based technique.[178,179] This methodology uses measured ventricular activity normalized for the acquisition time per frame and the activity in a known volume from a peripheral venous blood sample. Estimation of left ventricular volume is calculated using the formula

$$\text{Volume} = K\,(\text{Corrected LV counts})/(\text{No. of cardiac cycles})(\text{Time/frame})(\text{Blood activity})$$

where K is a correction constant to adjust for attenuation, which is usually determined from a regression equation using contrast angiography as a reference. This usually suffices for most individuals who are of normal size and shape, heart size, etc. However, in some patients, it is necessary to correct for individual variations, which can be successfully done using a simple geometric technique.[180,181] Using these data, stroke volume and cardiac output can be calculated using radionuclide ventriculography.[182,183] When the tomographic technique is used, ventricular volume is usually calculated using a geometric technique. Knowing the pixel volume, the ventricular volume can be calculated by summing the number of pixels in each tomographic section in the left ventricular ROI. Values obtained using this technique correlate well with other techniques, and have the advantage of not requiring any correction for attenuation.[184]

Valvular regurgitation can be evaluated by calculating the ratio of left to right ventricular stroke counts.[185,186] Normally, the right and left ventricular stroke volumes are equal. However, in the presence of valvular regurgitation the stroke volume is greater in the ventricle with the affected valve. Ventricular stroke counts are obtained by subtracting the end-systolic from the end-diastolic frame, resulting in a stroke volume image. In this image, the activity in the left and right ventricular regions is proportional to their respective stroke volumes. These data can be expressed in terms of either the stroke volume ratio (LV stroke counts/RV stroke counts, normal value <1.2) or as the regurgitant fraction (LV-RV stroke counts/LV stroke counts ×100, normal value <20%). The systematic overestimation of this technique results from right atrial/right ventricular overlap. Assessment of valvular regurgitation using this technique is somewhat crude. It is not possible to detect mild regurgitation or clearly quantitate the severity of the regurgitation. In addition, the accuracy is increasingly compromised when the LVEF is ≤35%. Valvular regurgitation can also be estimated using Fourier amplitude images.[187]

Diastolic function can also be assessed by radionuclide ventriculography.[188] The variables used are the peak filling rate (PFR), measured as the slope of a third-order polynomial

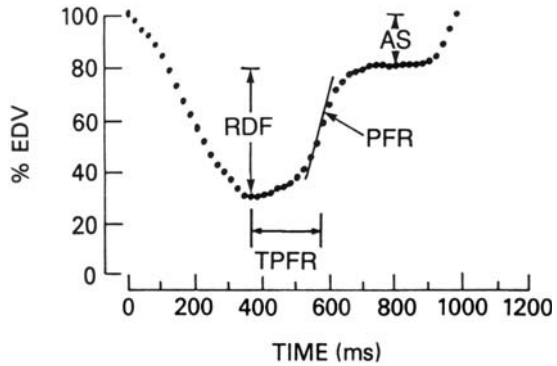

FIGURE 6.16. High temporal resolution time-activity curve obtained from radionuclide ventriculography. Each point represents 20 ms. Variables used to assess left ventricular rapid filling include peak filling rate (PFR), measured as the slope of a third-order polynomial fit to the rapid filling phase; time to peak filling rate (TPFR), measured from end-systole; and contributions of rapid diastolic filling (RDF) and atrial systole (AS), expressed as % of stroke volume. EDV, end-diastolic volume.

fit to the rapid filling phase, time to peak filling rate (TPFR), measured from end-systole, and the contribution of rapid diastolic filling (RDF) and atrial systole (AS) expressed as a percent of stroke volume (Fig. 6.16). However, noninvasive assessment of diastolic function, whether obtained using radionuclide or Doppler-echocardiographic techniques, has several limitations. These result from the dependence of these variables of diastolic function on other variables, such as heart rate, preload and afterload, and ejection fraction, making their interpretation difficult. Therefore, their clinical utility is limited. However, they may be helpful in patients with clinical features of cardiac failure but with a normal ejection fraction.

Regional ventricular function can be assessed either qualitatively or quantitatively using radionuclide ventriculography. The former method, using visual analysis of an endless-loop cine display, is the most widely used. There is good correlation between visual assessments of radionuclide and contrast ventriculograms, and reproducibility of the two techniques is comparable.[189,190] Quantitative techniques have been developed and can be broadly classified into geometric techniques (usually modifications of methods developed for contrast ventriculography) and nongeometric techniques specifically designed for radionuclide ventriculography.

The most commonly used nongeometric techniques use the regional ejection fraction and Fourier transform–derived phase and amplitude images. The regional ejection fraction image is obtained by subtracting the background-corrected end-systolic from the background-corrected end-diastolic frame.[191] The resulting image is normally crescent-shaped, delineating the left ventricular borders. If there is an area of regional hypokinesis or akinesis, there is thinning or absence of the crescent in this area. The data can also be presented in actual regional ejection fraction values with the left ventricle typically being divided into three or five segments.[192] Fourier phase analysis has been applied to the evaluation of radionuclide ventriculograms.[193] Each pixel has its own time-activity curve, which is maximal in end-diastole and at minimum in end-systole, whose fundamental frequency is determined by the heart rate. The time-activity curve is sinusoidal in shape and can be approximated using a single cosine function of the frequency of the time-activity curve. This allows each pixel within the region of the heart to be expressed as a single mathematical value, which can be color-coded. The amplitude of this cosine wave, equivalent to the change in counts during the cardiac cycle, is proportional to the stroke volume of the pixel. Therefore, the amplitude image gives a regional representation of stroke volume. For example, in a region of akinesis the pixels will show time-activity curves of reduced amplitude, resulting in the amplitude image showing absent activity in that region. The phase of the cosine wave can also be expressed in a similar fashion. The R-R interval is considered to represent 360 degrees, with the R wave occurring at 0 degrees, which coincides with the peak of the cosine wave. For pixels in areas of the ventricle where the onset of contraction is delayed, the peak of the cosine wave will also be delayed. This may be the result of either abnormal electrical activation or delayed onset of contraction, for example, myocardial ischemia or scarring. This delay can be expressed in terms of phase delay or increased phase angle. For example, an area of dyskinesis will result in a phase delay of around 180 degrees. Similarly, pixels in the atria have time-activity curves that are completely out of phase with the ventricles, equivalent to a phase delay of 180 degrees. These data can be expressed in a phase image, in which each pixel is color-coded according to its phase angle. Fourier images are useful in evaluating regional wall motion in patients with coronary artery disease at rest and exercise.[194–196] These images can also identify conduction abnormalities and have been used to localize the site of arrhythmias and also atrioventricular accessory pathways.[197–199]

Assessment of Right Ventricular Function

The complex geometry of the right ventricular poses major problems for all imaging modalities. However, radionuclide techniques are less geometrically dependent than other conventional imaging techniques, for example, contrast ventriculography or echocardiography, for the reasons discussed earlier. Three radionuclide techniques are used to assess right ventricular function. The first-pass technique, as described for the left ventricle, can be applied to the right ventricle.[200] This is probably the optimal technique for assessing right ventricular function, but suffers from the disadvantages as discussed previously. The gated equilibrium technique can also be used, but overlap of cardiac chambers is a significant limiting factor.[201–203] The right ventricular ejection fraction is calculated from the left anterior oblique projection, because this affords the best separation of the two ventricles. However, the right atrial and right ventricular overlap in this projection, resulting in a systematic underestimation of the right ventricular ejection fraction. Despite this, there is a good correlation with other methods of assessing right ventricular function using this technique.[204] A good compromise is the gated first-pass technique that involves injecting a bolus of ^{99m}Tc pertechnetate and acquiring

ECG-gated scintigraphic data from the time the bolus is seen entering the superior vena cava until it leaves the main pulmonary artery.[205] This gives excellent spatial resolution of the right atrium and right ventricle with no background contamination from lungs or the left heart chambers. Radioisotopes of inert noble gases, ^{81}Kr and ^{133}Xe, have also been used to assess right ventricular function.[206–209] These radioisotopes are rapidly excreted during their first passage through the lungs, allowing repeated studies to be performed without significantly increasing the radiation burden to the patient or problems of increasing background activity.

References

1. Gould KL, Lipscomb K, Hamilton GW. Physiologic basis for assessing critical coronary stenosis: instantaneous flow response and regional distribution during coronary hyperemia as measures of coronary flow reserve. Am J Cardiol 1974;33:87–94.
2. Holmberg S, Serzysko W, Varnauskas E. Coronary circulation during heavy exercise in control subjects and patients with coronary heart disease. Acta Med Scand 1971;190:465–480.
3. Heiss HW, Barmeyer J, Wink K, et al. Studies on the regulation of myocardial bloodflow in man: training effects on bloodflow and metabolism of the healthy heart at rest and during standardized heavy exercise. Basic Res Cardiol 1976;71:658–675.
4. Ferguson RJ, Cote P, Gauthier P, Bourassa MG. Changes in exercise coronary sinus blood flow with training in patients with angina pectoris. Circulation 1978;58:41–47.
5. Wilson RF, Laughlin DE, Ackell PH, et al. Transluminal, subselective measurement of coronary artery blood flow velocity and vasodilator reserve in man. Circulation 1985;72:82–92.
6. Rossen JD, Simonetti I, Marcus ML, Winniford MD. Coronary dilation with standard dose dipyridamole and dipyridamole combined with handgrip. Circulation 1989;79:566–572.
7. Gould KL. PET perfusion imaging and nuclear cardiology. J Nucl Med 1991;32:579–606.
8. Gould KL. Cardiac PET—state of the art. Circulation 1991; 84(suppl):1-22–1-36.
9. Gould KL. Percent coronary stenosis: Battered gold standard, pernicious relic, or clinical practicality? J Am Coll Cardiol 1988;11:886–888.
10. Marcus ML, Skorton DJ, Johnson MR, Collins SM, Harrison DG, Kerber RE. Visual estimates of percent diameter coronary stenosis: "a battered gold standard." J Am Coll Cardiol 1988; 4l:882–885.
11. White CW, Wright CB, Doty DB, et al. Does visual interpretation of the coronary arteriogram predict the physiologic importance of a coronary stenosis? N Engl J Med 1984;3l0:8l9–824.
12. Marcus ML, Harrison DG, White CW, McPherson DD, Wilson RF, Kerber RE. Assessing the physiologic significance of coronary obstructions in patients: Importance of diffuse undetected atherosclerosis. Prog Cardiol Dis 1988;3l:39–56.
13. Seiler C, Kirkeeide RL, Gould KL. Basic structure-function of the epicardial coronary vascular tree—the basis of quantitative coronary arteriography for diffuse coronary artery disease. J Clin Invest 1992;85:1987–2003.
14. Gould KL. Identifying and measuring the severity of coronary artery stenosis: quantitative coronary arteriography and positron emission tomography. Circulation 1988;68:237.
15. Gould KL. Quantitation of coronary stenosis in vivo. Circ Res 1985;57:341.
16. Kirkeeide RL, Gould KL, Parsel L. Assessment of coronary stenoses by myocardial perfusion imaging during pharmacologic coronary vasodilation, VII: validation of coronary flow reserve as a single integrated functional measure of stenosis severity reflecting all its geometric dimensions. J Am Coll Cardiol 1986;7:103.
17. Gould KL. Coronary Artery Stenosis. New York. Elsevier Scientific, 1990.
18. Gould KL, Kirkeeide R, Buchi M. Coronary flow reserve as a physiologic measure of stenosis severity, part I: relative and absolute coronary flow reserve during changing aortic pressure, part II: determination from the arteriographic stenosis dimensions under standardized conditions. J Am Coll Cardiol 1990; 15:459.
19. McCall D, Zimmer LJ, Katy AM. Kinetics of thallium exchange in cultured rat cells. Circ Res 1985;56:370–376.
20. Weich HF, Strauss HW, Pitt B. Extraction of thallium-201 by the myocardium. Circulation 1977;56:188–191.
21. Goldhaber SZ, Newell JB, Alpert NM, Andrews E, Pohost GM, Ingwall JS. Effects of ischemic-like insult on myocardial thallium-201 accumulation. Circulation 1983;67:778–786.
22. Leppo JA, MacNeil PB, Moring AF, Apstein CS. Separate effects of ischemia, hypoxia and contractility on thallium-201 kinetics in rabbit myocardium. J Nucl Med 1986;27:66–74.
23. Pohost GM, Alpert NS, Ingwall JS, Strauss HW. Thallium redistribution: mechanisms and clinical utility. Semin Nucl Med 1980;20:70–93.
24. Leppo JA. Myocardial uptake of thallium and rubidium during alterations in perfusion and oxygenation in isolated rabbit hearts. J Nucl Med 1987;28:878–885.
25. Strauss HW, Harrison K, Langan VK, Lebowitz E, Pitt B. Thallium-201 for myocardial imaging: relation of thallium-201 to regional myocardial perfusion. Circulation 1975;51:641–645.
26. Chu A, Murdock RH, Cobb FR. Relationship between regional distribution of thallium-201 and myocardial blood flow in normal, acutely ischemic and infarcted myocardium. Am J Cardiol 1982;50:1141–1144.
27. Nielsen AP, Morris KG, Murdock RH, Bruno FP, Cobb FR. Linear relationship between the distribution of thallium-201 and blood flow in ischemic and nonischemic myocardium during exercise. Circulation 1980;61:797–801.
28. Pohost GM, Okada RD, O'Keefe DD, et al. Thallium redistribution in dogs with severe coronary artery stenosis of fixed caliper. Circ Res 1981;48:439–446.
29. Gewirtz H, O'Keefe DD, Pohost GM, Strauss HW, McIlduff JB, Daggett WM. The effect of ischemia on thallium-201 clearance from the myocardium. Circulation 1978;58:216–219.
30. Kaul S, Chester DA, Pohost GM, Strauss HW, Okada RD, Boucher CA. Influence of peak exercise heart rate on normal thallium-201 myocardial clearance. J Nucl Med 1986: 2726–2730.
31. Brunken R, Tillisch J, Schwaiger M, et al. Regional perfusion, glucose metabolism, and wall motion in patients with chronic electrocardiographic Q wave infarctions: evidence for persistence of viable tissue in infarct regions by positron emission tomography. Circulation 1986;73:951–963.
32. Brunken R, Schwaiger M, Grover-McKay M, Phelps ME, Tillisch J, Schelbert HR. Positron emission tomography detects tissue metabolic activity in myocardial segments with persistent thallium perfusion defects. J Am Coll Cardiol 1987; 10:557–567.
33. Tillisch J, Brunken R, Marshall R, et al. Reversibility of cardiac wall-motion abnormalities predicted by positron emission tomography. N Engl J Med 1986;314:884–888.
34. Dilsizian V, Rocco TP, Freedman NM, Leon M, Bonow RO. Enhanced detection of ischemic but viable myocardium by the reinjection of thallium after stress-redistribution imaging. N Engl J Med 1990;323:141–146.
35. Dilsizian V, Smeltzer WR, Freedman NM, Dextras R, Bonow RO. Thallium reinjection after stress-reinjection imaging: does

24 hour delayed imaging after reinjection enhance detection of viable myocardium? Circulation 1991;83:1247–1255.
36. Bonow RO, Dilsizian V, Cuocolo A, Bacharach SL. Identification of viable myocardium in patients with chronic coronary artery disease and left ventricular dysfunction: comparison of thallium scintigraphy with reinjection and PET imaging with ^{18}F-Fluorodeoxyglucose. Circulation 1991;83:26–37.
37. Perrone-Filardi P, Bacharach SL, Dilizian V, Maurea S, Frank JA, Bonow RO. Regional left ventricular wall thickening: relation to regional uptake of ^{18}Fluorodeoxyglucose and ^{201}Tl in patients with chronic coronary artery disease. Circulation 1992;86:1125–1137.
38. Kitsiou AN, Srinivasan G, Quyyumi AA, et al. Stress-induced reversible and mild-to-moderate irreversible thallium defects: are they equally accurate for predicting recovery of regional left ventricular function after revascularization? Circulation 1998;98:501–508.
39. Kahn JK, McGhie AI, Akers MS, et al. Quantitative rotational tomography with ^{201}Tl and ^{99m}Tc 2–methoxy-isobutyl-isonitrile. A direct comparison in normal individuals and patients with coronary artery disease. Circulation 1989;79:1282–1293.
40. Leppo JA, DePuey EG, Johnson LL. A review of cardiac imaging with sestamibi and teboroxime. J Nucl Med 1991;32: 2012–2022.
41. Leppo JA, Meerdink DJ. Comparative myocardial extraction of two technetium-labeled BATO derivatives (SQ30217, SQ32014) and thallium. J Nucl Med 1990;31:67–74.
42. Gray WA, Gewirtz H. Comparison of ^{99m}Tc-Teboroxime with thallium for myocardial imaging in the presence of a coronary stenosis. Circulation 1991;84:1796–1807.
43. Stewart RE, Heyl B, O'Rourke RA, Blumhardt R, Miller DD. Demonstration of differential post-stenotic myocardial technetium-99m teboroxime clearance kinetics after experimental ischemia and hyperemic stress. J Nucl Med 1991; 32:2000–2008.
44. Beanlands R, Muzik O, Nguyen N, Petry N, Schwaiger M. The relationship of the myocardial retention of technetium-99m teboroxime and myocardial blood flow. J Am Coll Cardiol 1992;20:712–719.
45. Fleming RM, Kirkeeide RL, Taegtmeyer H, Adyanthaya A, Cassidy DB, Goldstein RA. Comparison of technetium-99m teboroxime and thallium-201 tomography with automated coronary arteriography and thallium tomographic imaging. J Am Coll Cardiol 1991;17:1297–1302.
46. Beller GA, Sinusas AJ. Experimental studies of the physiologic properties of technetium-99m isonitriles. Am J Cardiol 1990;66:5E–8E.
47. Beanlands RS, Dawood F, Wen WH, et al. Are the kinetics of Technetium-99m methoxyisobutyl isonitrile affected by cell metabolism and viability? Circulation 1990;82:1802–1814.
48. Carvalho PA, Chui ML, Kronauge JF, et al. Subcellular distribution and analysis of technetium-99m-MIBI in isolated perfused rat hearts. J Nucl Med 1992;33:1516–1522.
49. Kiat H, Maddahi J, Roy L, Friedman J, Berman DS. Comparison of Tc-99m-methoxyisobutyl isonitrile with Tl-201 imaging by planar and SPECT techniques for assessment of coronary disease. Am Heart J 1989;117:1–11.
50. Heller GV, Stowers SA, Hendel RC, et al. Clinical value of acute rest technetium-99m tetrofosmin tomographic myocardial perfusion imaging in patients with acute chest pain and nondiagnostic electrocardiograms. J Am Coll Cardiol 1998;31: 1011–1017.
51. Bilodeau L, Theroux P, Gregoire J, et al. Technetium-99m sestamibi tomography in patients with spontaneous chest pain: correlations with clinical, electrocardiographic and angiographic findings. J Am Coll Cardiol 1991;18:1684–1691.
52. Varetto T, Cantalupi D, Altieri A, et al. Emergency room technetium-99m sestamibi imaging to rule out acute myocardial ischemic events in patients with nondiagnostic electrocardiograms. J Am Coll Cardiol 1993;22:1804–1808.
53. Duca MD, Giri S, Wu AH, et al. Comparison of acute rest myocardial perfusion imaging and serum markers of myocardial injury in patients with chest pain syndromes. J Nucl Cardiol 1999;6:570–576.
54. Verani MS, Jeroudi MO, Mahmarian JJ, et al. Quantification of myocardial infarction during coronary occlusion and myocardial salvage after reperfusion using cardiac imaging with technetium-99m hexakis 2–methoxy isobutyl isonitrile. J Am Coll Cardiol 1988;12:1573–1581.
55. Sinusas AJ, Trautman KA, Bergin JD, et al. Quantification of area at risk during coronary occlusion and degree of myocardial salvage after reperfusion with technetium-99m methoxyisobutyl isonitrile. Circulation 1990;82:1424–1437.
56. Germano G, Kiat H, Kavanagh PB, et al. Automatic quantification of ejection fraction from gated myocardial perfusion SPECT. J Nucl Med 1995;36:2138–2147.
57. DePuey EG, Rozanski A. Using gated technetium-99m sestamibi SPECT to characterize fixed myocardial defects as infarct or artifact. J Nucl Med 1995;36:952–955.
58. Berman DS, Kiat HS, Van Train KF, et al. Myocardial perfusion imaging with technetium-99m-sestamibi: comparative analysis of available imaging protocols. J Nucl Med 1994;35:681–688.
59. Younes A, Songadele JA, Maublant J, et al. Mechanism of uptake of technetium-tetrofosmin. II: uptake into isolated adult rat heart mitochondria [published erratum appears in J Nucl Cardiol 1995;2:560]. J Nucl Cardiol 1995;2:327–333.
60. Platts EA, North TL, Pickett RD, Kelly JD. Mechanism of uptake of technetium-tetrofosmin. I: uptake into isolated adult rat ventricular myocytes and subcellular localization [published erratum appears in J Nucl Cardiol 1995;2:560]. J Nucl Cardiol 1995;2:316–326.
61. Kelly JD, Forster AM, Higley B, et al. Technetium-99m-tetrofosmin as a new radiopharmaceutical for myocardial perfusion imaging. J Nucl Med 1993;34:222–227.
62. Sinusas JA, Shi Q, Saltzberg MT, et al. Technetium-99m-tetrofosmin to assess myocardial blood flow: experimental validation in an intact canine model of ischemia. J Nucl Med 1994;35:664–671.
63. Munch G, Neverve J, Matsunari I, et al. Myocardial technetium-99m-tetrofosmin and technetium-99m-sestamibi kinetics in normal subjects and patients with coronary artery disease. J Nucl Med 1997;38:428–432.
64. Glover DK, Ruiz M, Yang JY, et al. Myocardial 99m-Tc-tetrofosmin uptake during adenosine-induced vasodilatation with either a critical or mild coronary stenosis: comparison with 2–1Tl and regional myocardial blood flow. Circulation 1997; 96:2332–2338.
65. Shanoudy H, Raggi P, Beller GA, et al. Comparison of technetium-99m-tetrofosmin and thallium-201 single-photon emission computed tomographic imaging for detection of myocardial perfusion defects in patients with coronary artery disease. J Am Coll Cardiol 1998;31:331–337.
66. Matsunari I, Fujino S, Taki J, et al. Comparison of defect size between thallium-201 and technetium-99m tetrofosmin myocardial single-photon emission computed tomography in patients with single-vessel coronary artery disease. Am J Cardiol 1996;77:350–354.
67. Tamaki N, Takahashi N, Kawamoto M, et al. Myocardial tomography using technetium-99m-tetrofosmin to evaluate coronary artery disease. J Nucl Med 1994;35:594–600.
68. Rigo P, Leclercq B, Itti R, et al. Technetium-99m-tetrofosmin myocardial imaging: a comparison with thallium-201 and angiography. J Nucl Med 1994;35:587–593.

69. Zaret BL, Rigo P, Wackers FJ, et al. Myocardial perfusion imaging with 99mTc tetrofosmin: comparison to 201 Tl imaging and coronary angiography in a phase III multicenter trial. Tetrofosmin International Trial Study Group [see comments]. Circulation 1995;91:313–319.
70. Acampa W, Cuocolo A, Sullo P, et al. Direct comparison of technetium 99m-sestamibi and technetium 99m-tetrofosmin cardiac single photon emission computed tomography in patients with coronary artery disease. J Nucl Cardiol 1998;5:265–274.
71. Higginbotham MB. Cardiac performance during submaximal and maximal exercise in healthy persons. Heart Failure 1988; 4:68–76.
72. Leppo JA. Dipyridamole-Thallium imaging: the lazy man's stress test. J Nucl Med 1989;30:281–287.
73. Beller GA. Pharmacologic stress imaging. JAMA 1991;265: 633–638.
74. Ranhosky A, Kempthorne-Rawson J, and the Intravenous Dipyridamole Thallium Imaging Study Group. The safety of intravenous dipyridamole thallium myocardial perfusion imaging. Circulation 1990;81:1205–1209.
75. Miura M, Tominago S, Hashimoto K. Potentiation of reactive hyperemia in the coronary and femoral circulation by the selective use of 2, 5–bis-(diethanolamino)-4,8–dipiperidino (5,4–d) pyrimidine. Arzneium-Forschrift 1967;17:976–979.
76. Kubler W, Bretschneider HJ. Competitive inhibition of catalyzed adenosine diffusion as the mechanism of coronary dilating action of a pyrimido-pyrimidine derivative. Pflugers Arch 1964;280:141–157.
77. Afonso S, O'Brien GS. Mechanism of enhancement of adenosine action by dipyridamole and lidoflazine in dogs. Arch Int Pharmacodyn Ther 1971;194:181–196.
78. Fenton RA, Bruttig SP, Rubio R, Berne RM. Effect of adenosine on calcium uptake by intact and cultured vascular smooth muscle. Am J Physiol 1987;252:H598–604.
79. Fredholm BB, Gustafsson LH, Hedqvist P, Sollevi A. Adenosine in the regulation of neurotransmitter release in the peripheral nervous system. In: Berne RM, Rall TW, Rubio R, eds. Regulatory Function of Adenosine. The Hague: Martinus Nijhoff, 1983:479–495.
80. Rovetto MJ. Myocardial nucleotide transport. Am Rev Physiol 1985;47:605–616.
81. Hiefsen-Kadsk F, Pedersen AK. Pharmacokinetics of dipyridamole. Acta Pharmacol Toxicol 1979;44:391–399.
82. Fredholm BB, Persson CG. Xanthine derivatives and adenosine receptor antagonists. Eur J Pharmacol 1981;81:673–676.
83. Wilson RF, Wychek K, Christensen BV, Zimmer S, Laxson DD. Effects of adenosine on human coronary arterial circulation. Circulation 1990;82:1595–1606.
84. Christensen CW, Rosen LB, Gal RA, Haseeb M, Lassar TA, Port SC. Coronary vasodilator reserve: comparison of the effects of papaverine and adenosine on coronary flow, ventricular function, and myocardial metabolism. Circulation 1991;83: 294–303.
85. Verani MS, Mahmarian JJ, Hixson JB, Boyce TM, Staudacher RA. Diagnosis of coronary artery disease by controlled coronary vasodilation with adenosine and Thallium-201 scintigraphy in patients unable to exercise. Circulation 1990; 82:80–87.
86. Coyne EP, Belvedere DA, Vande Streek PR, Weiland FL, Evans BB, Spaccavento LJ. Thallium-201 scintigraphy after intravenous infusion of adenosine compared with exercise: Thallium testing in the diagnosis of coronary artery disease. J Am Coll Cardiol 1991;17:1289–1294.
87. Nishimura S, Mahmanian JJ, Boyce TM, Verani MS. Quantitative Thallium-201 single photon emission computed tomography during maximal pharmacologic coronary vasodilation with adenosine for assessing coronary artery disease. J Am Coll Cardiol 1991;18:736–745.
88. Abreu A, Mahmarian JJ, Nishimura S, Boyce TM, Verani M. Tolerance and safety of pharmacologic coronary vasodilation with adenosine in association with thallium-201 scintigraphy in patients with suspected coronary artery disease. J Am Coll Cardiol 1991;18:730–735.
89. Glover DK, Ruiz M, Yang JY, et al. Pharmacological stress thallium scintigraphy with 2–(cyclohexylmethylidene)hydrazinoadenosine (WRC-0470), a novel, short-acting adenosine A_{2A} receptor agonist. Circulation 1996;94:1726–1732.
90. Bertolet BD, Belardinelli L, Franco EA, et al. Selective attenuation by N-0861 (N^{6-}endonorbornan-2–yl-9–methyladenine) of cardiac A_1 adenosine receptor-mediated effects in humans. Circulation 1996;93:1871–1876.
91. Udelson JE, Heller GV, Wackers FJT, et al. Randomized, controlled dose-ranging study of the selective adenosine A2A receptor agonist binodenoson for pharmacological stress as an adjunct to myocardial perfusion imaging. Circulation 2004; 109:457–464.
92. Gould KL, Westcott RJ, Albro PC, Hamilton GW. Non-invasive assessment of coronary stenosis by myocardial imaging during pharmacologic coronary vasodilation II: clinical methodology and feasibility. Am J Cardiol 1978;41:279–287.
93. Casale PN, Guiney TE, Strauss HW, Boucher CA. Simultaneous low-level treadmill exercise and intravenous dipyridamole stress thallium imaging. Am J Cardiol 1988;62:799–802.
94. Brown G, Josephesen MA, Petersen RB, et al. Intravenous dipyridamole combined with isometric handgrip for near maximal acute increase in coronary flow in patients with coronary artery disease. Am J Cardiol 1981;48:1077–1085.
95. Stern S, Greenberg ID, Corne R. Effect of exercise supplementation on dipyridamole Thallium-201 image quality. J Nucl Med 1991;32:1559–1564.
96. De Puey EG. Exercise supplementation of dipyridamole for myocardial perfusion imaging. J Nucl Med 1991;32:1564–1568.
97. Ruffolo RR. Review: the pharmacology of dobutamine. Am J Med Sci 1987;294:244–248.
98. Meyer SL, Curry GC, Donsky MS, Twieg DB, Parkey RW, Willerson JT. Influence of dobutamine on hemodynamics and coronary flow in patients with and without coronary artery disease. Am J Cardiol 1976;38:103–108.
99. Willerson JT, Hutton I, Watson JT, Platt MR, Templeton GH. Influence of dobutamine on regional myocardial bloodflow and ventricular performance during acute and chronic myocardial ischemia in dogs. Circulation 1976;53:828–833.
100. McGillem MJ, Scott BS, DeBoe SF, Friedman HZ, Mancini GBJ. The effects of dopamine and dobutamine on regional function in the presence of rigid coronary stenoses and subcritical impairments of reactive hyperemia. Am Heart J 1988;115: 970–977.
101. Fung AY, Gallagher KP, Buda AJ. The physiologic basis of dobutamine as compared with dipyridamole stress interventions in the assessment of critical coronary stenosis. Circulation 1987;76:943–951.
102. Pennell DJ, Underwood SR, Swanton RH, Walker JM, Ell PJ. Dobutamine thallium myocardial perfusion tomography. J Am Coll Cardiol 1991;18:1471–1479.
103. Elliot BM, Robison JG, Zellner JL, Hendrix GH. Dobutamine-201Tl imaging: assessing cardiac risks associated with vascular surgery. Circulation 1991;84(suppl 5):III-54–60.
104. Marwick T, Willemart B, D'Hondt AM, et al. Selection of the optimal nonexercise stress for the evaluation of ischemic regional myocardial dysfunction and malperfusion: comparison of dobutamine and adenosine using echocardiography and 99mTc-MIBI single photon emission computed tomography. Circulation 1993;87:345–354.

105. Hays JT, Mahmarian JJ, Cochran AJ, et al. Dobutamine thallium-201 tomography for evaluating patients with suspected coronary disease unable to undergo exercise or vasodilator pharmacologic stress testing. J Am Coll Cardiol 1993;21: 1583–1590.
106. DePuey EG, Garcia EV. Updated Imaging Guidelines For Nuclear Cardiology Procedures, Part 1. J Nuc Cardiol 2001;8: G5–G58.
107. Fintel DJ, Links JM, Brinker JA, Frank TL, Parker M, Becker L. Improved diagnostic performance of exercise thallium-201 single photon emission computed tomography over planar imaging in the diagnosis of coronary artery disease: a receiver operating characteristic analysis. J Am Coll Cardiol 1989; 13:600–612.
108. Berman DS, Kiat H, Friedman JD, et al. Separate acquisition rest thallium-201/stress technetium-99m sestamibi dual-isotope myocardial perfusion single-photon emission tomography: a clinical validation study. J Am Coll Cardiol 1993;22: 1455–1464.
109. Berman DS, Hachamovich R, Kiat H, et al. Incremental value of prognostic testing in patients with known or suspected ischemic heart disease: a basis for optimal utilization of exercise technetium-99m sestamibi myocardial perfusion single-photon emission computed tomography. J Am Coll Cardiol 1995;26: 639–647.
110. Clausen M, Bice AN, Civelek C, Hutchins GM, Wagner HN. Circumferential wall thickness measurements of the human left ventricle: reference data for thallium-201 single photon emission computed tomography. Am J Cardiol 1986;58:827–831.
111. Garcia EV, Van Train K, Maddahi J, et al. Quantification of rotational Thallium-201 myocardial tomography. J Nucl Med 1985;26:17–26.
112. DePasquale EE, Nody AC, DePuey EG, et al. Quantitative rotational thallium-201 tomography for identifying and localizing coronary artery disease. Circulation 1988;77:316–327.
113. Maddahi J, Van Train K, Prigent F, et al. Quantitative single photon emission computed thallium-201 tomography for detection and localization of coronary artery disease: Optimization and prospective validation of a new technique. J Am Coll Cardiol 1989;14:1689–1699.
114. DePuey EG, Garcia EV. Optimal specificity of thallium-201 SPECT through the recognition of imaging artifacts. J Nucl Med 1989;30:441–449.
115. Kiat H, Van Train KF, Friedman JD, et al. Quantitative stress-redistribution imaging thallium-201 SPECT using prone imaging: methodologic development and validation. J Nucl Med 1992;33:1509–1515.
116. Cooper JA, Neumann PH, McCandless BK. Effect of patient motion on tomographic myocardial perfusion imaging. J Nucl Med 1992;33:1566–1571.
117. Matzer L, Kiat H, Friedman JD, Van Train K, Maddahi J, Berman DS. A new approach to the assessment of tomographic thallium-201 scintigraphy in patients with left bundle branch block. J Am Coll Cardiol 1991;17:1309–1317.
118. Wintergreen Summary: Panel on Instrumentation and Quantification. J Nucl Cardiol 1999;6:94–103.
119. Germano G, Erel J, Kiat H, et al. Quantitative LVEF and qualitative regional function from gated thallium-201 perfusion SPECT. J Nucl Med 1997;38:749–754.
120. Ficaro EP, Fessler JA, Shreve PD, et al. Simultaneous transmission emission myocardial perfusion: diagnostic accuracy of attenuation-corrected 99mTc-sestamibi, single-photon emission computed tomography. Circulation 1996;93:463–473.
121. Ficaro EP, Fessler JA, Ackermann RJ, et al. Simultaneous transmission-emission thallium-201 cardiac SPECT: effect of attenuation correction on myocardial tracer distribution. J Nucl Med 1995;36:921–931.
122. Kluge R, Sattler B, Seese A, et al. Attenuation correction by simultaneous emission-transmission myocardial single-photon emission tomography using a technetium-99m-labelled radiotracer: impact on diagnostic accuracy. Eur J Nucl Med 1997;24:1107–1114.
123. Gallowitsch HJ, Sykora J, Mikosch P, et al. Attenuation-corrected thallium-201 single-photon emission tomography using a gadolinium-153 moving line source: clinical value and the impact of attenuation correction on the extent and severity of perfusion abnormalities. Eur J Nucl Med 1998; 25:220–228.
124. Hendel RC, Berman DS, Cullom SJ, et al. Multicenter clinical trial to evaluate the efficacy of correction for photon attenuation and scatter in SPECT myocardial perfusion imaging. Circulation 1999;99:2742–2749.
125. Links JM, Becker LC, Rigo P, et al. Combined corrections for attenuation, depth-dependent blur, and motion in cardiac SPECT: a multicenter trial. J Nucl Cardiol 2000;7:414–425.
126. Duvernoy CS, Ficaro EP, Karabajakian MZ, et al. Improved detection of left main coronary artery disease with attenuation-corrected SPECT. J Nucl Cardiol 2000;7:639–648.
127. Klocke FJ, Baird MG, Bateman TM, et al. AHA/AHA/ASNC Guidelines for the Clinical Use of Cardiac Radionuclide Imaging. A Report of the American College of Cardiology/ American Heart Association Task Force on Practice Guidelines. http://www.acc.org/clinical/guidelines/radio/rni_fulltext.pdf, accessed April 16, 2005.
128. Hendel RC, Corbett JR, Cullom SJ, et al. The value and practice of attenuation correction for myocardial perfusion SPECT imaging: a joint position statement from the American Society of Nuclear Cardiology and the Society of Nuclear Medicine. J Nucl Cardiol 2002;9:135–143.
129. Bacharach SL. The new-generation positron emission tomography/computed tomographic scanners: implications for cardiac imaging. J Nucl Cardiol 2004;11:388–392.
130. Bergmann SR, Fox KAA, Rand AL, et al. Quantification of regional myocardial blood flow in vivo with $H_2{}^{15}O$. Circulation 1984;70:724–728.
131. Knabb RM, Fox KAA, Sobel BE, et al. Characterization of the functional significance of subcritical stenosis with $H_2{}^{15}O$ and positron emission tomography. Circulation 1985;71:1271–1282.
132. Nienaber CA, Ratib O, Gambhir S, et al. A quantitative index of regional blood flow in canine myocardium derived noninvasively with N-13 ammonia and dynamic positron emission tomograph. J Am Coll Cardiol 1991;17:260–269.
133. Schelbert HR, Wisenberg G, Phelps ME, et al. Non-invasive assessment of coronary stenosis by myocardial imaging during pharmacologic coronary vasodilation. VI. Detection of coronary artery disease in man with intravenous N-13 ammonia and positron computed tomography. Am J Cardiol 1982;49: 1197–1207.
134. Gould KL, Goldstein RA, Mullani NA. Economic analysis of clinical positron emission tomography of the heart with rubidium-82. J Nucl Med 1989;30:707–717.
135. Schelbert HR, Phelps ME, Huang S, et al. N-13 ammonia as an indicator of myocardial blood flow, Circulation 1981;63: 1259–1271.
136. Krivokapich J, Huang SC, Selin CE, et al. Fluorodeoxyglucose rate constants, lumped constant, and glucose metabolic rate in rabbit heart. Am J Physiol 1987;252:H777–H787.
137. Ratib O, Phelps, ME, Huang SC, et al. Positron emission tomography with deoxyglucose for estimating local myocardial glucose metabolism. J Nucl Med 1982;23:577–586.
138. Schon H, Schelbert HR, Najafi A, et al. C-11–labeled palmitic acid for noninvasive evaluation of regional myocardial fatty acid metabolism with positron computed tomography. II.

Kinetics of C-11–palmitic acid in acutely ischemic myocardium. Am Heart J 1982;1103:548–561.
139. Schelbert HR, Henze E, Schon H, et al. C-11–labeled palmitic acid for noninvasive evaluation of regional myocardial fatty acid metabolism with positron computed tomography. III. In vivo demonstration of the effects of substrate availability on myocardial metabolism. Am Heart J 1983;105: 492–504.
140. Sobel BE, Geltman EM Tiefenbrunn AJ, et al. Improvement of regional myocardial metabolism after coronary thrombolysis induced with tissue-type plasminogen activator or streptokinase. Circulation 1984;69:983–990.
141. Bergmann SR, Lerch RA, Fox KAA, et al. Temporal dependence of beneficial effects of coronary thrombolysis characterized by positron emission tomography. Am J Med 1982;73:573–581.
142. Knabb RM, Bergmann SR, Fox KAA, et al. The temporal pattern of recovery of myocardial perfusion and metabolism delineated by positron emission tomography following coronary thrombolysis. J Nucl Med 1987;28:1563–1570.
143. Schelbert HR, Henze E, Schon H, et al. C-11–labeled palmitic acid for noninvasive evaluation of regional myocardial fatty acid metabolism with positron computed tomography. III. In vivo demonstration of the effects of substrate availability on myocardial metabolism. Am Heart J 1983;105:492–504.
144. Schon H, Schelbert HR, Najafi A, et al. C-11–labeled palmitic acid for noninvasive evaluation of regional myocardial fatty acid metabolism with positron computed tomography. II. Kinetics of C-11–palmitic acid in acutely ischemic myocardium. Am Heart J 1982;1103:548–561.
145. Brown M, Myears D, Bergmann S. Validity of estimates of myocardial oxidative metabolism with carbon-11–acetate and positron emission tomography despite altered patterns of substrate utilization. J Nucl Med 1989;30:187–193.
146. Brown M, Marshall D, Sobel B. Delineation of myocardial oxygen utilization with carbon-11–labeled acetate. Circulation 1987;76:687–696.
147. Brown M, Myears D, Bergmann S. Noninvasive assessment of canine myocardial oxidative metabolism with carbon-11–acetate and positron emission tomography. J Am Coll Cardiol 1988;12:1054–1063.
148. Walsh M, Geltman E, Brown M, et al. Noninvasive estimation of regional myocardial oxygen consumption by positron emission tomography with carbon-11–acetate in patients with myocardial infarction. J Nucl Med 1989;30:1798–1808.
149. Buxton DB, Nienaber CA, Luxen A, et al. Noninvasive quantitation of regional myocardial oxygen consumption in vivo with [1–11C] acetate and dynamic positron emission tomography. Circulation 1989;79:134–142.
150. Armbrecht JJ, Buxton DB, Schelbert HR. Validation of [1–11C] acetate kinetics as a tracer for noninvasive assessment of oxidative metabolism with positron emission tomography in normal, ischemic, postischemic, and hyperemic canine myocardium. Circulation 1990;81:1594–1605.
151. Lear JL. Relationship between myocardial clearance rates of carbon-11–acetate-derived radiolabeled and oxidative metabolism: physiologic basis and clinical significance (editorial). J Nucl Med 1991;32:1957–1060.
152. McCord ME, Bacharach SL, Bonow RO, Dilsizian V, Cuocolo A, Freedman N. Misalignment between PET transmission and emission scans: its effect on myocardial imaging. J Nucl Med 1992;33:1209–1213.
153. Shelbert HR, Wisenberg G, Phelps ME, et al. Non-invasive assessment of coronary artery stenoses by myocardial perfusion imaging during pharmacologic coronary vasodilation: VI. Detection of coronary artery disease in human beings with intra-venous N-13 ammonia and positron emission tomography. Am J Cardiol 1982;49:1197–1201.
154. Tamaki N, Yonekura Y, Senda M, et al. Value and limitation of stress 201Tl single photon emission tomography: comparison with nitrogen-13 ammonia positron emission tomography. J Nucl Med 1988;29:1181–1188.
155. Demer LL, Gould KL, Goldstein RA, et al. Assessment of coronary artery disease severity by positron emission tomography: comparison with quantitative coronary arteriography in 193 patients. Circulation 1989;79:825–835.
156. Go RT, Marwick TH, MacIntyre WJ, et al. A prospective comparison of rubidium-82 PET and thallium-210 SPECT myocardial perfusion imaging utilizing a single dipyridamole stress in the diagnosis of coronary artery disease. J Nucl Med 1990; 31:1899–1905.
157. Stewart RE, Schwaiger M, Molina E, et al. Comparison of rubidium-82 positron emission tomography and thallium-201 SPECT imaging for detection of coronary artery disease. Am J Cardiol 1991;67:1303–1310.
158. Bonow RO, Berman DS, Gibbons RJ, et al. Cardiac positron emission tomography: a report for health professionals from the Committee on Advanced Cardiac Imaging and Technology on Clinical Cardiology, American Heart Association. Circulation 1991;84:447–454.
159. Bateman TM, Heller GV, McGhie AI, Friedman JD, Case JA, Bryngelson JR, Hertenstein GK, Moutray KL, Reid KJ, Collum SJ. Diagnostic Accuracy of Rest/Stress ECG-gated Rubidium-82 Myocardial Perfusion PET: Comparison with ECG-gated Tc-99m-Sestamibi SPECT. J Nucl Cardiol 2006;13:24–33.
160. Watson DD, Nelson JP, Gottlieb S. Rapid bolus injection of radioisotopes. Radiology 1973;106:347–352.
161. Berger JH, Mathay RA, Pytlik LM, Gottschalk A, Zaret BL. First-pass radionuclide assessment of right and left ventricular performance in patients with cardiac and pulmonary disease. Semin Nucl Med 1979;9:275–224.
162. Dymond DS, Elliot AT, Flatman W, et al. The clinical validation of gold-195m: a new short half-life radiopharmaceutical for rapid, sequential, first pass angiocardiography. J Am Coll Cardiol 1983;2:85–92.
163. Wackers FJ, Stein R, Pytlik L, et al. Gold-195m for serial first pass radionuclide angiocardiography during upright exercise in patients with coronary artery disease. J Am Coll Cardiol 1983;2:497–505.
164. Jones RH. Radionuclide angiocardiography. In: Marcus, Schelbert, Skorton, Wolf, eds. Cardiac Imaging—Principles and Practice. Philadelphia: WB Saunders, 1991:1006–1026.
165. Askenazi J, Amnberg DS, Korngold E, LaFarge CG, Maltz DL, Treves S. Quantitative radionuclide angiocardiography. Am J Cardiol 1976;97:382–387.
166. Treves S, Collins-Nakai RL. Radioactive tracers in congenital heart disease. Am J Cardiol 1976;38:711–721.
167. Gilday DL, DeSouza M. Pediatric nuclear cardiology. In: Come PC, ed. Diagnostic Cardiology, Noninvasive Imaging Techniques. Philadelphia: JB Lippincott, 1985:159–190.
168. Peter CA, Armstrong BE, Jones RH. Radionuclide quantitation of right-to-left intracardiac shunts in children. Circulation 1981;64:572–577.
169. Corbett JR, Jansen DE, Lewis SE, et al. Tomographic gated blood pool radionuclide ventriculography: analysis of wall motion and left ventricular volumes in patients with coronary artery disease. J Am Coll Cardiol 1985;6:349–358.
170. Gill JB, Moore RH, Tamaki N, et al. Multi-gated blood-pool tomography: new method for the assessment of left ventricular function. J Nucl Med 1986;12:1916–1924.

171. Maublant J, Bailly P, Mestas D, et al. Feasibility of gated single photon transaxial tomography of the cardiac blood pool. Radiology 1983;146:837–839.
172. Poliner LR, Dehmer GJ, Lewis SE, Parkey RW, Blomqvist CG, Willerson JT. Left ventricular performance in normal subjects: a comparison of the responses to exercise in the upright and supine position. Circulation 1980;62:528–534.
173. Manyari DE, Kostuk WJ. Left and right ventricular function at rest and during bicycle exercise in the supine and sitting positions in normal subjects and patients with coronary artery disease. Am J Cardiol 1983;51:36–42.
174. Freeman MR, Berman DS, Staniloff H, et al. Comparison of upright and supine bicycle exercise in the detection and evaluation of extent of coronary artery disease by equilibrium radionuclide ventriculography. Am Heart J 1981;102:182–189.
175. Higgenbotham MB, Morris KG, Coleman E, Cobb FR. Sex-related differences in normal cardiac response to upright exercise. Circulation 1984;70:357–366.
176. Hanley PJ, Gibbons RJ, Zinsmeister AR, et al. Sex-related differences in cardiac response to supine exercise assessed by radionuclide angiography. J Am Coll Cardiol 1989;13: 624–629.
177. Parker JA, Secker-Walker R, Hill R, Siegel BA, Potchen EJ. A new technique for the calculation of left ventricular ejection fraction. J Nucl Med 1972;13:585–592.
178. Dehmer GJ, Lewis SE, Hillis LD, et al. Nongeometric determination of left ventricular volumes from equilibrium blood pool scans. Am J Cardiol 1980;45:293–300.
179. Dehmer GJ, Firth BG, Hillis LD, Nicod P, Willerson JT, Lewis SE. Nongeometric determinations of right ventricular volumes from equilibrium blood pool scans. Am J Cardiol 1982; 49:78–84.
180. Links JM, Becker LC, Shindledecker JG, et al. Measurement of absolute left ventricular volumes from gated blood pool studies. Circulation 1982;65:82–91.
181. Starling MR, Dell'Italia LJ, Walsh RA, Little WC, Benedetto AR, Nusynowitz ML. Accurate estimates of absolute left ventricular volumes from equilibrium radionuclide angiographic count data using a simple geometric attenuation correction. J Am Coll Cardiol 1984;3:789–798.
182. Dehmer GJ, Firth BG, Lewis SE, Willerson JT, Hillis LD. Direct measurement of cardiac output by gated equilibrium blood pool scintigraphy: validation of scintigraphic volume measurements by a non-geometric technique. Am J Cardiol 1981;47: 1061–1067.
183. Konstam MA, Wynne J, Holman BL, Brown EJ, Neill JM, Kolowski RT. Use of equilibrium (gated) radionuclide ventriculography to quantitate left ventricular output in patients with and without left-sided valvular regurgitation. Circulation 1981;64:578–585.
184. Corbett JR, Jansen DE, Lewis SE, et al. Tomographic gated blood pool radionuclide ventriculography: analysis of wall motion and left ventricular volumes in patients with coronary artery disease. J Am Coll Cardiol 1985;6: 349–358.
185. Rigo P, Alderson PO, Robertson RM, Becker LC, Wagner HN. Measurement of aortic and mitral regurgitation by gated blood pool scans. Circulation 1979;60:306–312.
186. Nicod P, Corbett JR, Firth BG, et al. Radionuclide techniques for valvular regurgitation index: comparison in patients with normal or depressed ventricular function. J Nucl Med 1982; 23:763–769.
187. Makler PT, McCarthy DM, Velchik MG, Goldstein HA, Alavi A. Fourier amplitude ratio: a new way to assess valvular regurgitation. J Nucl Med 1983;24:204–207.
188. Bonow RO. Radionuclide angiographic evaluation of left ventricular diastolic function. Circulation 1991;84(suppl I): I-208–I215.
189. Okada RD, Kirshenbaum HD, Kushner FG, et al. Observer variance in the qualitative evaluation of left ventricular wall motion and the quantitation of left ventricular ejection fraction using rest and exercise multigated blood pool imaging. Circulation 1980;61:128–136.
190. Okada RD, Pohost GM, Nichols AB, et al. Left ventricular regional wall motion assessment by multigated and end-diastolic, end-systolic gated radionuclide left ventriculography. Am J Cardiol 1980;45:1211–1218.
191. Maddox DE, Holman BL, Wynne J, et al. Ejection fraction image: a non-invasive index of regional left ventricular wall motion. Am J Cardiol 1978;14:1230–1238.
192. Maddox DE, Wynne J, Uren R, et al. Regional ejection fraction: a quantitative radionuclide index of regional left ventricular performance. Circulation 1979;59:1001–1009.
193. Links LM, Douglass KH, Wagner HN. Patterns of ventricular emptying by Fourier analysis of gated blood-pool studies. J Nucl Med 1980;21:978–982.
194. Ratib O, Henze E, Schon H, Schelbert H. Phase analysis of radionuclide ventriculograms for the detection of coronary artery disease. Am Heart J 1982;104:1–12.
195. Walton S, Yiannikas J, Jarritt PH, Brown NJG, Swanton RH, Ell PJ. Phasic abnormalities of left ventricular emptying in coronary artery disease. Br Heart J 1981;46:250–253.
196. Bacharach SL, Green MV, Bonow RO, DeGraaf CN, Johnston GS. A method for objective evaluation of functional images. J Nucl Med 1982;23:285–290.
197. Links JM, Raichlen JS, Wagner HN, Reid PR. Assessment of the site of ventricular activation by Fourier analysis of gated blood pool studies. J Nucl Med 1985;26:27–32.
198. Botvinick E, Dunn R, Frais M, et al. The phase image: its relationship to patterns of contraction and conduction. Circulation 1982;65:551–560.
199. Botvinick E, Frais M, O'Connell W, et al. Phase image evaluation of patients with ventricular pre-excitation syndromes. J Am Coll Cardiol 1984;3:799–814.
200. Berger JH, Mathay RA, Pytlik LM, Gottschalk A, Zaret BL. First-pass radionuclide assessment of right and left ventricular performance in patients with cardiac and pulmonary disease. Semin Nucl Med 1979;9:275–294.
201. Maddahi J, Berman DS, Masouka DT, et al. A new technique for assessing right ventricular ejection fraction using rapid multiple-gated equilibrium cardiac blood pool scintigraphy. Description, validation and findings in chronic coronary artery disease. Circulation 1979;60:581–589.
202. Rigo P, Murray M, Taylor D, et al. Right ventricular dysfunction in patients with acute inferior infarction. Circulation 1975;32:268–274.
203. Slutsky R, Hooper W, Gerber K. Assessment of right ventricular function at rest and during exercise in patients with coronary heart disease: a new approach using equilibrium radionuclide ventriculography. Am J Cardiol 1980;45:63–71.
204. Starling MR, Dell'Italia LJ, Chaudhuri TK, Boros BL, O'Rourke RA. First transit and equilibrium radionuclide angiocardiography in patients with inferior transmural myocardial infarction: criteria for diagnosis of associated hemodynamically significant right ventricular infarction. J Am Coll Cardiol 1984; 4:923–930.
205. Winzelberg CG, Boucher CA, Pohost GM, et al. Right ventricular function in aortic and mitral disease: relation of gated first-pass radionuclide angiography to clinical and hemodynamic findings. Chest 1981;79:520–528.

206. Goldberg MJ, Mantel J, Freidin M, Ruskin R, Rubentire M. Intravenous xenon-133 for determination of radionuclide first pass right ventricular ejection fraction. Am J Cardiol 1981; 47:626–630.
207. Martin W, Tweddel A, McGhie I, Hutton I. Gated Xenon scans for right ventricular function. J Nucl Med 1986;27:609–615.
208. McGhie I, Martin W, Tweddel A, Hutton I. Assessment of right ventricular function in acute inferior myocardial infarction using 133–Xenon imaging. Int J Cardiol 1989; 22:195–202.
209. Ham HR, Piepz A, Vandevivere J, Guillaume M, Goethals P, Lenaers A. The evaluation of right ventricular performance using krypton-81m. Clin Nucl Med 1983;8:257–260.